ALD GROWN ZNO AS AN ALTERNATIVE MATERIAL FOR PLASMONIC AND UNCOOLED INFRARED IMAGING APPLICATIONS

A THESIS

SUBMITTED TO THE DEPARTMENT OF ELECTRICAL AND

ELECTRONICS ENGINEERING

AND THE GRADUATE SCHOOL OF ENGINEERING AND SCIENCE

OF BILKENT UNIVERSITY

IN PARTIAL FULFILLMENT OF THE REQUIREMENTS

FOR THE DEGREE OF

MASTER OF SCIENCE

By

Yunus Emre Kesim

June, 2014

I certify that I have read this thesis and that in my opinion it is fully adequate, in scope and in quality, as a thesis for the degree of Master of Science.

Asst. Prof. Dr. Ali Kemal Okyay(Advisor)

I certify that I have read this thesis and that in my opinion it is fully adequate, in scope and in quality, as a thesis for the degree of Master of Science.

Prof. Dr. Ayhan Altıntaş

I certify that I have read this thesis and that in my opinion it is fully adequate, in scope and in quality, as a thesis for the degree of Master of Science.

Prof. Dr. Mehmet Bayındır

Approved for the Graduate School of Engineering and Science:

Prof. Dr. Levent Onural
Director of the Graduate School

ABSTRACT

ALD GROWN ZNO AS AN ALTERNATIVE MATERIAL FOR PLASMONIC AND UNCOOLED INFRARED IMAGING APPLICATIONS

Yunus Emre Kesim
M.S. in Electrical and Electronics Engineering
Supervisor: Asst. Prof. Dr. Ali Kemal Okyay
June, 2014

Plasmonics is touted as a milestone in optoelectronics as this technology can form a bridge between electronics and photonics, enabling the integration of electronics and photonic circuits at the nanoscale. Noble metals such as gold and silver have been extensively used for plasmonic applications due to their ability to support plasmons, yet they suffer from high intrinsic optical losses. Recently, there is an increased effort in the search for alternative plasmonic materials including Si, Ge, III-Nitrides and transparent conductive oxides. The main appeal of these materials, most of them semiconductors, is their lower optical losses, especially in the infrared (IR) regime, compared to noble metals owing to their lower number of free electrons. Other advantages can be listed as low-cost and control on plasma frequency thanks to the tunable electron concentration, i.e. effective doping level.

This work focuses on atomic layer deposition (ALD) grown ZnO as a candidate material for plasmonic applications. Optical constants of ZnO are investigated along with figures of merit pertaining to plasmonic waveguides. It is shown that ZnO can alleviate the trade-off between propagation length and mode confinement width owing to tunable dielectric properties. In order to demonstrate plasmonic resonances, a grating structure is simulated using finite-difference-time-domain (FDTD) method and an ultra-wide-band (4-15 μm) infrared absorber is computationally demonstrated.

Finally, an all ZnO microbolometer is proposed, where ALD grown ZnO is employed as both the thermistor and the absorber of the microbolometer which is an uncooled infrared imaging unit that relies on the resistance change of the active material (thermistor) as it heats up due to the absorption of incident electromagnetic radiation. The material complexity and process steps of microbolometers

could be reduced if the thermistor layer and the absorber layer were consolidated in a single layer. Computational analysis of a basic microbolometer structure using FDTD method is conducted in order to calculate the absorptivity in the long-wave infrared (LWIR) region (8-12 μm). In addition, thermal simulations of the microbolometer structure are conducted using finite element method, and time constant and noise-equivalent-temperature-difference (NETD) values are extracted.

Keywords: Plasmonics, alternative plasmonic materials, transparent conductive oxides, metal oxides, ZnO, atomic layer deposition, FDTD method, uncooled infrared imaging, microbolometer, all-ZnO microbolometer.

ÖZET

PLAZMONİK VE SOĞUTMASIZ KIZILÖTESİ GÖRÜNTÜLEME UYGULAMALARI İÇİN ALTERNATİF MALZEME OLARAK ATOMİK KATMAN KAPLAMA YÖNTEMİ İLE BÜYÜTÜLMÜŞ ÇİNKO OKSİT

Yunus Emre Kesim
Elektrik ve Elektronik Mühendisliği, Yüksek Lisans
Tez Yöneticisi: Yrd. Doç. Dr. Ali Kemal Okyay
Temmuz, 2014

Elektronik ve fotonik arasında bir köprü kurarak elektronik ve fotonik devrelerin nano boyutlarda entegrasyonunu sağlayabileceği için, plazmonik konusu optoelektronik alanında bir kilometre taşı olmuştur. Altın ve gümüş gibi soy metaller plazmonik uygulamalarda sıklıkla kullanılsalar da yüksek miktardaki optik kayıplardan etkilenirler. Son zamanlarda; Si, Ge, III-Nitrrler ve saydam iletken oksitler gibi alternatif plazmonik malzemeler üzerine çalışmalar yoğunlaşmıştır. Çoğu yarı iletken olan bu malzemelerin en çekici yanı, metallere nazaran daha az sayıda serbest elektronları olması nedeniyle özellikle kızılötesi (IR) dalgaboylarında daha az kayıplarının olmasıdır. Diğer avantajlar ise düşük maliyet ve ayarlanabilir elektron sayısı (efektif katkılama yoğunluğu) sayesinde plazma frekansının kontrol edilebilmesi olarak sıralanabilir.

Bu çalışmada atomik katman kaplama yöntemi ile büyütülmüş ZnO malzemesinin plazmonik uygulamalara uygunluğu incelenmiştir. Çinko oksitin optik sabitleri ve plazmonik dalga kılavuzu başarım ölçüleri araştırılmıştır. Çinko oksitin ayarlanabilir dielektrik özellikleri sayesinde, yayılım uzunluğu ve biçim hapsedilme genişliği arasındaki getiri-götürü dengesini ayarlayabileceği gösterilmiştir. Plazmonik rezonansları göstermek içinse zaman alanında sonlu farklar yöntemi (FDTD) kullanılarak bir optik ızgara yapısının simülasyonu yapılmış, ultra-geniş bant aralığında (4-15 μm) çalışan bir emici elde edilmiştir.

Son olarak, elektromanyetik yayılımın emilmesinden kaynaklı ısı artışının sebep olduğu direnç değişikliğine bağlı olarak çalışan bir soğutmasız kızılötesi

görüntüleme birimi olan, çinko oksitin hem termistör hem de emici olarak kullanıldığı tamamen çinko oksitten oluşan bir mikrobolometre önerilmiştir. Termistör ve emici katmanlar tek bir katmanda birleştirildiği takdirde, mikrobolometrelerin malzeme karışıklığı ve üretim süreci adımları azalacaktır. Uzun dalga (LWIR) kızılötesi (8-12 μm) dalgaboylarındaki emilim miktarının hesaplanabilmesi için basit bir mikrobolometre yapısı FDTD yöntemi kullanılarak incelenmiştir. Ayrıca, sonlu eleman yöntemi kullanılarak mikrobolometre yapısının termal simulasyonları yapılmış, gürültüye denk sıcaklık farkı (NETD) ve zaman sabiti değerleri bulunmuştur.

Anahtar sözcükler: Plazmonik, alternatif plazmonik malzemeler, saydam iletken oksitler, metal oksitler, çinko oksit, atomik katman kaplama, FDTD yöntemi, soğutmasız kızılötesi görüntüleme, mikrobolometre, tamamen çinko oksit mikrobolometre.

Acknowledgement

If you fail to attain self knowledge,
What good is there in your studies?
Yunus Emre ($13^{th} - 14^{th}$ centuries)

I would like to express my gratitude to my thesis supervisor, Dr. Ali Kemal Okyay for his support and guidance. I consider myself lucky for working with him for the past seven years at Bilkent University.

I would like to thank Prof. Ayhan Altıntaş and Prof. Mehmet Bayındır for being in my thesis committee.

I would like to acknowledge support from TÜBİTAK-BİDEB national MS Fellowship program. This work was supported by the Scientific and Technological Research Council of Turkey (TÜBİTAK), grant numbers 109E044, 112M004, 112E052, 113M815 and 113M912.

I want to extend my thanks to Sami Bolat and Enes Battal for their friendship and useful discussions through this work. I also want to thank Dr. M. Yusuf Tanrikulu for the thermal simulations and contributions in this thesis.

I would like to thank friends I made at UNAM. Firstly, I want to thank Oğuz Hanoğlu: Aside from being the person who introduced me to research, he has been an inspiration. I would like to thank Ali Cahit Kösger who was my mentor in the laboratories. I want to thank members of Okyay Group: Burak Tekcan, Fatih Bilge Atar, Levent Erdal Aygün, Amir Ghobadi, Amin Nazirzadeh, Muhammad Maiz Ghauri, Ayşe Özcan and Feyza Bozkurt Oruç. I also want to thank Aziz Karaşahin.

I owe many thanks to my coworkers at ASELSAN: I want to thank Dr. Süleyman Umut Eker for being always supportive and understanding, Alp Tolungüç for his friendship and teaching materials science to me, and Melih Kaldırım for being the guy who knows everything and always eager to answer questions.

I want to thank my friends at ASELSAN for sharing their experiences related to both academic and non-academic life with me: Murat Celal Kılınç, Ayşe Begüm Arığ Çelik and Ferhat Taşdemir. Special thanks goes to Neslihan Çiçek (Demirer) for being a role-model to me since high school.

The last two years at Bilkent would be unbearable unless I had two special people alonside with me: Hüseyin Gürkan, who motivated me to pursue a Ph.D. abroad; and Oğuz Çetin, whom I persuaded for a Ph.D. abroad. I also want to thank Arif Usta, Fatih Çalışır, Serkan Pekçetin, Murat İplikçi and Onursal Bağırgan for all the great time we had on the football pitch.

Although this research is conducted in the last two years, my adventure at Bilkent dates back to 2007. I want to thank Emre Gökçe, Tayfun Arıcı, Tuna Kalınsaz, Mesut Çamlı, Doğan Çalışgan and Mehmet Ali Salman for their friendship. I also want to thank Caner Orhan, Caner Odabaş, Fırat Yılmaz and Emin Çelik.

There are some people in my life who knows me better than myself: Dr. Gürkan Bektaş, Dr. Melik Kayıkçı and Dr. Rıfat Göde. I also want to thank Dr. Selim Turan and Dr. İbrahim Erol for their support and friendship.

I do not know a word that could express my feelings towards my family, let alone English, even in Turkish. All I can say is that the motivation of my life is trying to be the person worthy of their love.

Dedicated to my brother Yasin and my loving parents…

Contents

List of Figures

List of Tables

Chapter 1

Introduction

Developments in complementary-metal-oxide-semiconductor (CMOS) technology provides microprocessors with tiny transistors. Intel's Haswell series microprocessors employ transistors with 22 nm channel length. 14 nm channel length Broadwell series is announced. Such scaling down in the size of the microelectronic components enabled us faster data processing at smaller volumes. Today's smartphones are employing quad-core processors and operating at over 2.5 GHz.

Although microelectronics is capable of processing vast data, transfer of information is becoming more difficult with increasing resistance of the smaller electronic interconnects. The RC time constant sets the upper limit of the bandwidth of information transfer in digital circuits.

On the other hand, photonics offer much higher data transfer rates. Google Fiber offers its customers 1 Gbps internet connection. However, the disadvantage of the optical interconnects are their larger size compared to electronic counterparts. Because of the diffraction limit, optical devices are at sizes comparable to the wavelength they operate (at the μm scale). The fiber optic communication operates at 1.55 μm wavelength.

Under right conditions, incident light on an interface between a metal and a dielectric can excite resonances in the mobile electrons (plasma) at the surface of

the metal. Such resonances are called the surface plasmons [1]. As the resonances are taking place at an interface, plasmonics promise subwavelength confinement of light, into nano dimensions. As a result, high speed data transfer rates of optical interconnects can be achieved at nano-sized components similar to electronics.

Although first observed by Robert Wood in 1902 [2], plasmonics attracted more interest since the Thomas Ebbesen's paper in 1998 [3]. Potential of merging electronics and photonics at nanoscale dimensions attracted interest of researchers [4]. Confinement of field also results in very high electromagnetic enhancement in the near field [5]. Therefore, plasmonics enables much stronger interaction between light and matter and many applications can take the advantage of this property. Today applications of plasmonics span a wide range including sub-wavelength waveguiding [6], imaging [7] and lithography [8]; optical interconnects [9] and photonic circuits [10]; chemical and biological sensors [11, 12]; improved photovoltaic devices [13, 14] and perfect absorbers [15, 16].

1.1 Alternative Plasmonic Materials

The metal is essential for plasmonic applications as it is the material that supports the surface plasmons. Although noble metals such as gold and silver are widely used in plasmonic applications [17], there is a significant drawback associated with such metals:high optical loss due to the very high number of free electrons and interband transitions [18]. Loss is associated with the imaginary part of the relative permittivity of the metal (ϵ_r''). The smaller ϵ_r'' yields lower loss. Relative permittivity of some metals are given in Figure 1.1 (adapted from [19]). According to Drude model, which will be discussed in Chapter 2 in more detail, imaginary part of the permittivity of metal is given by

$$\epsilon_r'' = \frac{\omega_p^2 \gamma}{\omega(\omega^2 + \gamma^2)} \tag{1.1}$$

where ω_p is the plasma frequency of the metal and γ is the damping rate which is on the order of a few THz. Therefore at optical frequencies ($\omega \ll \gamma$), (1.1) can

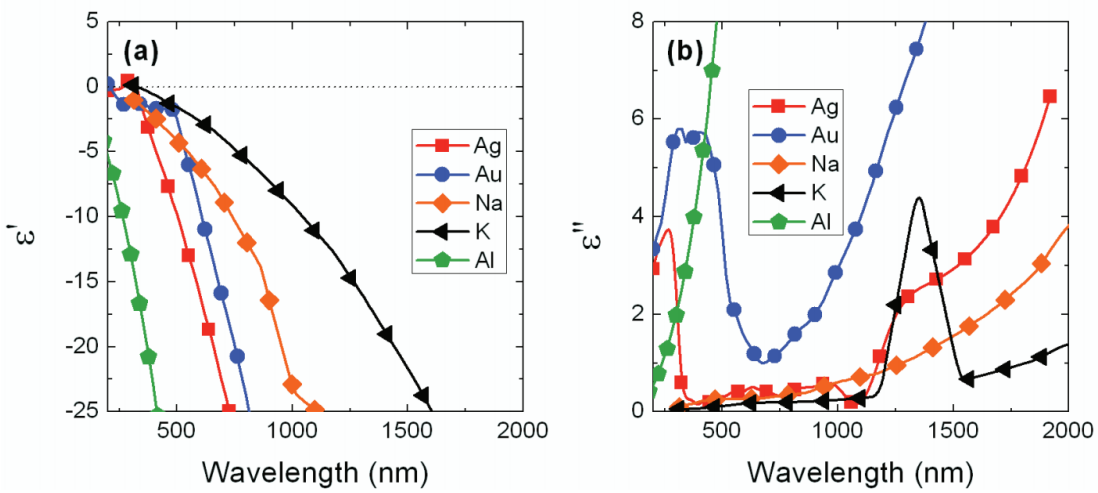

Figure 1.1: Relative permittivity of Au, Ag, Al, Na and K in the visible and the near-infrared. Although Na and K achieve lower losses, they are not preferred as they react with water and air.

be approximated as

$$\epsilon_r'' = \frac{\omega_p^2 \gamma}{\omega^3} \tag{1.2}$$

Equation (1.2) shows that in order to reduce optical losses in plasmonic materials, one should be able to reduce either the plasma frequency or the damping rate. The latter is related to the electron scattering mechanisms in the metal [17] which is a function of temperature. By cooling to cryogenic temperatures ($< 100°K$), damping rate can be reduced and therefore lower loss could be achieved [20]. Yet, this is not a practical solution for many reasons (need for coolers etc.).

A better approach would be trying to reduce the plasma frequency which is given by

$$\omega_p = \sqrt{\frac{Ne^2}{\epsilon_o m}} \tag{1.3}$$

where N is the free electron concentration of metal, ϵ_o is vacuum permittivity, e and m are electron charge and effective mass, respectively. (1.3) shows that plasma frequency is only a function of the free electron density. However, N depends on the material and therefore cannot be adjusted for metals. On the other hand, for semiconductors it is trivial (to some extent) to adjust the electron density via doping. This is the main motivation behind employing semiconductors

in plasmonic applications and this study.

Besides lower loss, there are other advantages of semiconductors over metals. First of all, since the plasma frequency is a function of doping concentration, the dielectric constant of semiconductors can be tuned depending on the application. For example, two important figures of merit defined for plasmonic materials are the plasmon propagation length and the mode confinement width. As it will be shown theoretically in Chapter 2, there is a trade of between these two figures. Although for a certain metal they are constant, it is possible to fine tune when the plasmonic material is a semiconductor [21].

Another advantage of semiconductors in plasmonic applications arises from their compatibility with well established CMOS processes. Gold and silver diffuses into Si and these impurities introduce acceptor/donor levels within the bandgap of Si [22]. As a result, the electronic performance of Si based devices are affected. On the other hand, semiconductors like TaN and TiN are demonstrated as plasmonic materials and their usage as gate materials in CMOS devices is also reported [23].

The reasons discussed above encouraged scientists to seek alternative plasmonic materials. Although various metals, metal alloys and intermetallics are examined as well, research focused on transition metal nitrides, semiconductors and graphene [19].

1.1.1 Transition Metal Nitrides

TiN, ZrN, HfN and TaN shows metallic properties [19] and they are shown as alternative plasmonic materials in the visible and the near infrared (Figure 1.2 [24]. The main advantage of these materials, as mentioned above, is their compatibility with the CMOS procedures, which makes them prime candidates for the integration of plasmonics with Si electronics. Also, they can be grown under either nitrogen rich or metal rich conditions and the latter results in films that show more metallic properties. Hence, the plasma frequency can be tuned.

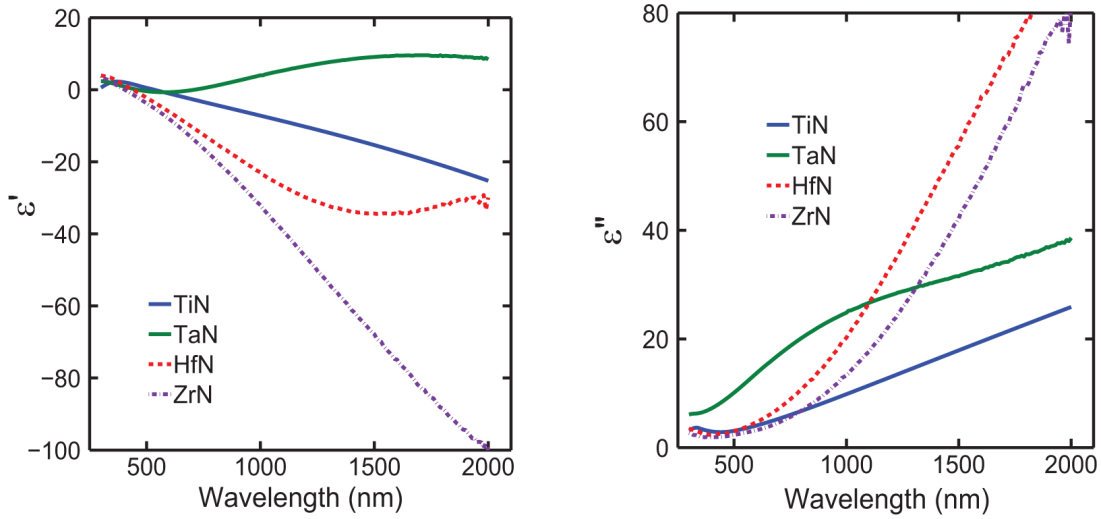

Figure 1.2: Relative permittivity of metal nitrides: TiN, TaN, ZrN, HfN in the visible and the near infrared. Since $\epsilon' < 0$, they are possible plasmonic materials in this wavelength range.

1.1.2 Semiconductors

To employ semiconductors as plasmonics materials, heavy doping is required since the plasma frequency depends on the electron density. Therefore, only semiconductors with high solid solubility levels can be used as plasmonic materials. Also, as the interband transitions causes absorption and results in loss, semiconductors with high bandgap energies are more advantageous.

1.1.2.1 Silicon

Today's CMOS technology depends on Si. Using Si as a plasmonic material would be a big step towards integrating electronic and photonic circuits. Also, with a bandgap energy of 1.12 eV, interband transitions are not allowed for $\lambda > 1.1$ μm. Due to these properties, silicon plasmonics drew interest [25–28].

Using (1.3), carrier density levels (N) required in order to achieve plasma frequencies (f) that correspond to various wavelengths are calculated (Table 1.1). Note that the plasma frequency is given as the ordinary frequency in Hz, not the

radial frequency (rad/s). The electron effective mass in Si is $1.18 \times m_o$ where m_o is the electron mass [29].

$\epsilon' < 0$ for wavelengths larger than that corresponding to the plasma frequency. Therefore, in order to achieve a plasmonic material that will operate in mid infrared ($\lambda > 5\mu m$), required doping density is on the order of 10^{19} and it is larger for near infrared and visible regimes (Table 1.1). Most commonly used n type dopants in Si are P and As with solid solubility of $1.82 \times 10^{21}\ cm^{-3}$ and $1.56 \times 10^{21}\ cm^{-3}$, respectively [30]. Although these values seem to be sufficient compared to Table 1.1, as the dopant concentration gets closer to the solubility limit, defect densities increases which results in more scattering. Therefore, Si can be an effective alternative plasmonic material only at the mid-infrared and beyond.

1.1.2.2 Germanium

Ge is getting more and more integrated to Silicon technology as it serves as absorber with 0.66 eV bandgap energy. Monolithic Ge/Si avalanche photodiodes with large gain/bandwidth products are reported [31]. On the other hand, low bandgap energy is not preferable for plasmonic applications as it increases loss.

Required doping densities for plasmonic applications of Ge is about half of that of Si due to the lower effective electron mass in Ge (Table 1.1) [29]. However, solid solubility limits for antimony, which is the most common n type dopant, in Ge is around $1.56 \times 10^{19}\ cm^{-3}$ [30]. Therefore, Ge can be a plasmonic material only at the far infrared.

1.1.2.3 GaAs

GaAs is widely used both for optoelectronic and power electronics applications. It has a much lower electron effective mass ($0.066 \times m_o$, [29])compared to Si and Ge which results in an order of magnitude lower carrier concentration that is required (Table 1.1).

Si is commonly used for n type doping, but it has also an acceptor level within the bandgap of GaAs. Although the solid solubility limit is higher, effective n type doping of GaAs using Si can reach 10^{19} cm^{-3}. Beyond this level, amphoteric property of Si causes the compensation as some of the Si impurities behave as acceptors [19]. Therefore, similar to Si, GaAs can be used as a plasmonic material only at the mid-infrared and beyond.

Table 1.1: Carrier density levels (in cm^{-3}) required to achieve various plasma wavelengths. The values were found using the equation for plasma frequency (1.3).

λ	500 (nm)	1550 (nm)	5000 (nm)
Si	5.27×10^{21}	5.48×10^{20}	5.27×10^{19}
Ge	2.45×10^{21}	2.55×10^{20}	2.45×10^{19}
GaAs	2.94×10^{20}	3.06×10^{19}	2.94×10^{18}

1.1.2.4 Transparent Conductive Oxides

Transparent conductive oxides (TCOs) show metallic properties as they can be doped at very high levels [19]. Also, having a large bandgap energy makes them transparent in the visible region. Therefore, interband transitions are very low which in turn yields lower loss.

Indium-tin-oxide (ITO) is widely investigated as an alternative plasmonic material both in near and mid infrared [24,32–36]. The concentration of oxygen vacancies affect the optical properties of ITO: oxygen rich films have higher carrier densities yielding in a more metallic behavior [19]. Therefore, by annealing ITO under oxygen rich or deficient atmosphere, one can adjust the free carrier density and in turn the plasma frequency. Such tuning of plasma frequency is desirable as it gives an upper hand while balancing the trade off between surface plasmon propagation length and mode confinement width.

ZnO is also widely investigated as a candidate plasmonic material. Aluminum doped zinc oxide (AZO) [37] and gallium doped zinc oxide (GZO) are shown to have similar properties with ITO as seen in Figure 1.3 which is adapted from [24].

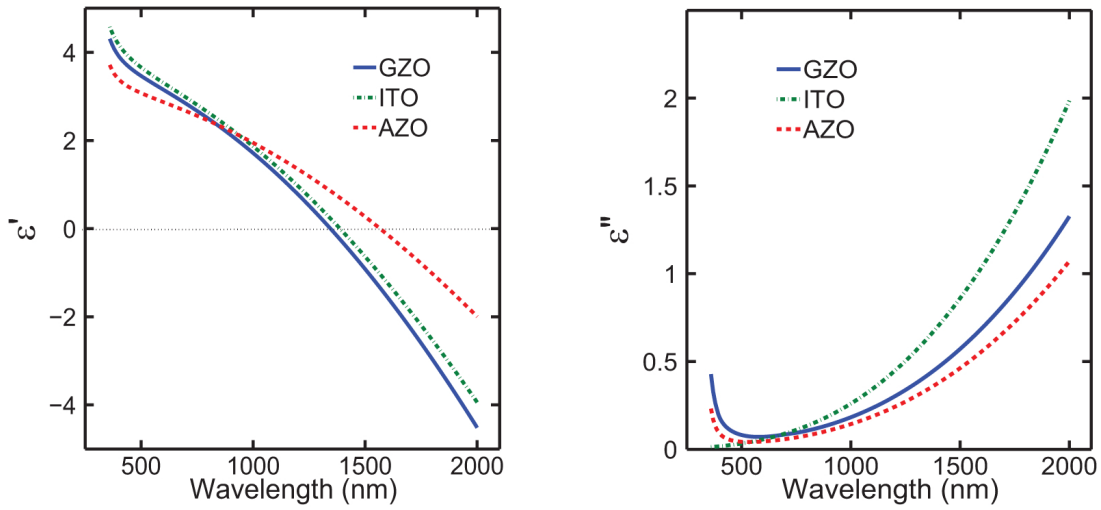

Figure 1.3: Relative permittivity of common transparent conductive oxides: ITO, AZO and GZO

Similar to ITO, zinc oxide also employs oxygen vacancies as n type dopants. Therefore, by changing the growth conditions the material can be tuned.

This work also investigates atomic layer deposition (ALD) grown ZnO as a candidate plasmonic material.

1.1.3 Graphene

Graphene and plasmonics, two very interesting subjects in the field of photonics have overlapped. Several groups demonstrated plasmonic resonances in graphene at THz and infrared regimes [38–42].

Unlike the materials discussed so far, graphene employs 2D electron plasma which results in different physical phenomena and optical properties. Even the plasmon dispersion relation is different [42]. As the case for 2D materials is completely a new discipline, further discussion of graphene plasmonics is out of scope of this thesis.

1.2 Thesis Organization

In this first chapter, the field of plasmonics and its promises are briefly introduced. The need for the alternative plasmonic materials is discussed and a literature review of alternative plasmonic materials is presented.

The organization of the rest of the thesis is as follows:

In Chapter 2, the theoretical electromagnetic background will be given. Starting with Maxwell's equations, wave equation and surface plasmons will be derived. Also, the physics behind the response of materials to electromagnetic fields will be described. Lorentzian and Drude models are going to be presented.

In Chapter 3, ALD grown ZnO will be investigated as an alternative plasmonic material. ALD growth and ellipsometer characterization of ZnO will be presented.

In Chapter 4, finite-difference-time-domain (FDTD) simulations regarding two distinct applications of ALD grown ZnO will be presented. First one is an ultra-wide band infrared absorber that utilizes ZnO plasmonic gratings. The main motivation of this work is computationally demonstrating the plasmonic resonances at ZnO. Finaly, an all-ZnO microbolometer for uncooled infrared imaging will be computationally demonstrated. Optical and thermal simulations of this microbolometer will be described.

Chapter 5 concludes this thesis and discusses potential future directions.

Chapter 2

Background

In order to understand plasmonics, it is very important to comprehend the fundamental concepts in electromagnetics and optics. Therefore, in this chapter we start by reviewing Maxwell's equations. We investigate a material's response to incident electromagnetic field and explain the physics behind it. Finally, plasma oscillations of metals under electric field i.e. plasmons are presented.

2.1 Maxwell's Equations

The relations and variations of the electric and magnetic fields, charges, and currents associated with electromagnetic waves are governed by Maxwell's equations [43]. In a source-free medium, the electric and magnetic field vectors satisfy the following equations:

$$\nabla \times \mathcal{H} = \frac{\partial \mathcal{D}}{\partial t} \tag{2.1}$$

$$\nabla \times \mathcal{E} = -\frac{\partial \mathcal{B}}{\partial t} \tag{2.2}$$

$$\nabla \cdot \mathcal{D} = 0 \tag{2.3}$$

$$\nabla \cdot \mathcal{B} = 0 \tag{2.4}$$

where $\mathcal{E}$ is *electric field*, $\mathcal{H}$ is *magnetic field*, $\mathcal{D}$ is *electric flux density* and $\mathcal{B}$ is *magnetic flux density*. Flux density vectors can be expressed as:

$$\mathcal{D} = \epsilon_o \mathcal{E} + \mathcal{P} \tag{2.5}$$

$$\mathcal{B} = \mu_o \mathcal{H} + \mu_o \mathcal{M} \tag{2.6}$$

where ϵ_o and μ_o are the permittivity and permeability of free space, respectively. $\mathcal{P}$ is *polarization density* and $\mathcal{M}$ is *magnetization density*. In non-magnetic medium, $\mathcal{M} = 0$. In linear, nondispersive (memoryless), homogeneous and isotropic media $\mathcal{E}$ and $\mathcal{P}$ are parallel and proportional and are related by:

$$\mathcal{P} = \epsilon_o \chi \mathcal{E} \tag{2.7}$$

where χ is a material dependent scalar named *electric susceptibility*. Substituting (2.7) into (2.5), $\mathcal{D} = \epsilon_o \mathcal{E} + \epsilon_o \chi \mathcal{E}$ we find:

$$\mathcal{D} = \epsilon \mathcal{E} \tag{2.8}$$

$$\mathcal{B} = \mu_o \mathcal{H} \tag{2.9}$$

where ϵ is defined as the *electric permittivity* of the medium. Ratio of electric permittivity of medium to that of free space is called *dielectric constant* (*relative permittivity*) of the material and denoted by ϵ_r:

$$\epsilon = \epsilon_o (1 + \chi) \tag{2.10}$$

$$\epsilon_r = 1 + \chi \tag{2.11}$$

Substituting (2.8) and (2.9) into (2.1)-(2.4) we end up with the Maxwell's equations in source free, non-magnetic, linear, nondispersive, homogeneous and isotropic media:

$$\nabla \times \mathcal{H} = \epsilon \frac{\partial \mathcal{E}}{\partial t} \tag{2.12}$$

$$\nabla \times \mathcal{E} = -\mu_o \frac{\partial \mathcal{H}}{\partial t} \tag{2.13}$$

$$\nabla \cdot \mathcal{E} = 0 \tag{2.14}$$

$$\nabla \cdot \mathcal{H} = 0 \tag{2.15}$$

First applying curl on both sides of (2.13) then substituting (2.12) into (2.13) and using vector identity $\nabla \times \nabla \times \mathcal{E} = \nabla(\nabla \cdot \mathcal{E}) - \nabla^2\mathcal{E}$, one can reach the wave equation :

$$\nabla^2\mathcal{E} = \frac{1}{c^2}\frac{\partial^2\mathcal{E}}{\partial^2 t} \tag{2.16}$$

where c is the speed of light in the medium and can be written as

$$c = \frac{1}{\sqrt{\epsilon\mu_o}} \tag{2.17}$$

In free space, speed of light is $c_o = 1/\sqrt{\epsilon_o\mu_o}$ which roughly equals 3×10^8 m/s. The ratio of the speed of light in a medium to that of in free space is called the *refractive index* of the material and denoted by n:

$$n = \frac{c}{c_o} = \sqrt{\epsilon_r} \tag{2.18}$$

$$n = \sqrt{1 + \chi} \tag{2.19}$$

So far we assumed that the medium is fully transparent i.e. not absorbing the incident light. If the medium is absorbing, the optical constants defined above are not purely real numbers. The imaginary part of the constants are related to absorption:

$$\epsilon_r = \epsilon_r' - j\epsilon_r'' \tag{2.20}$$

$$\chi = \chi' - j\chi'' \tag{2.21}$$

$$\tilde{n} = n - jk \tag{2.22}$$

where ϵ_r' and χ' are the real parts of the dielectric constant and the susceptibility of the medium, respectively. Similarly, ϵ_r'' and χ'' are the imaginary counterparts. Notation is different for refractive index: $\tilde{n}$ denotes the *complex refractive index*, n and k denotes the real and imaginary parts, respectively. The relationship between dielectric constant and refractive index becomes:

$$\epsilon_r' = n^2 - k^2 \tag{2.23}$$

$$\epsilon_r'' = 2nk \tag{2.24}$$

Although we came up with several optical constants regarding the behavior of electromagnetic fields in a medium i.e. ϵ_r, χ, n ..., they are all related to each other and each of them is sufficient to describe a material's response to incident electromagnetic fields.

2.2 Plane Wave

In the previous section, the equation describing the waves in a medium is found (2.16). Electromagnetic waves in a medium have both time and space dependence. If we assume that the wave is a time-harmonic wave and the space dependence is only along the z axis, it can be written in the form

$$\mathcal{E}(z,t) = Re\{\mathcal{E}(z)e^{j\omega t}\} \tag{2.25}$$

If this equation is substituted into the wave equation, what we find is called the *Helmholtz equation* which describes the amplitude of the waves in a medium:

$$\nabla^2\mathcal{E}(z) - \mathbf{k}^2\mathcal{E}(z) = 0 \tag{2.26}$$

$$\mathbf{k} = \omega/c \tag{2.27}$$

where $\mathbf{k}$ is called the *complex wavevector* of the wave.

The simplest solution that satisfies the *Helmholtz equation* is given by

$$\mathcal{E}(z) = E_o e^{-j\mathbf{k}z} \tag{2.28}$$

where E_o is a complex number and defined as the *complex envelope* of the wave. The elecromagnetic wave defined by (2.28) is called the *plane wave*:

$$\mathcal{E}(z,t) = Re\{E_o e^{-j\mathbf{k}z} e^{j\omega t}\} \tag{2.29}$$

Using (2.18) and (2.27), we can define $\mathbf{k_o} = \mathbf{k}/\tilde{n}$ as the wavevector in the air or vacuum. Subtituting $\mathbf{k} = \tilde{n}\mathbf{k_o}$ and therefore $\mathbf{k} = \mathbf{k_o}(n - jk)$ into (2.29), we find

$$\mathcal{E}(z,t) = Re\{E_o e^{-k\mathbf{k_o}z} e^{-jn\mathbf{k_o}z} e^{j\omega t}\} \tag{2.30}$$

Propagation constant (β) and *absorption coefficient* (α) are defined as

$$\beta = n\mathbf{k_o} = \frac{2\pi}{\lambda_o}n \tag{2.31}$$

$$\alpha = 2k\mathbf{k_o} = \frac{4\pi}{\lambda_o}k \tag{2.32}$$

where λ_o is the wavelength of the wave in vacuum or air. (2.30) can be written as

$$\mathcal{E}(z,t) = Re\{E_o e^{-\alpha/2} e^{-j\beta z} e^{j\omega t}\} \tag{2.33}$$

Beer's law is related to how much the intensity of light is absorbed as it travels through a medium:

$$I(z) = I_o e^{-\alpha z} \tag{2.34}$$

Note that the intensity is the absolute square of the complex amplitude of the wave.

We shall end this section by analyzing what happens when a plane wave is normally incident at a plane boundary. Assume that a plane wave in a transparent medium 1 with $\tilde{n}_1 = n_1$ is normally incident to the planar boundary of medium 2 with $\tilde{n}_2 = n_2 - jk_2$. When an electromagnetic wave is incident at a boundary, a portion of the wave will be transmitted through the boundary while a portion will be reflected (Figure 2.1).

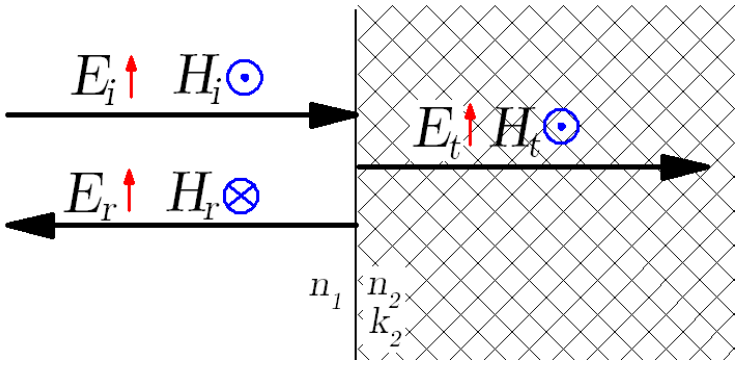

Figure 2.1: Normally incident light onto planar boundary: The incident, reflected and the transmitted waves are denoted with the obvious subscripts.

The boundary conditions require that the tangential component of the electric and magnetic field accross the boundary should be equal as there is no surface current. Therefore;

$$E_i + E_r = E_t \tag{2.35}$$

$$H_i - H_r = H_t \tag{2.36}$$

The *impedance* of a medium is defined as $Z = E/H$ where E and H are the complex amplitudes of the field within. Using Maxwell's equations, we can find

$$Z = \sqrt{\frac{\mu}{\epsilon}} \tag{2.37}$$

Therefore we can write (2.36) as

$$E_i - E_r = mE_t \tag{2.38}$$

where $m = \tilde{n}_2/\tilde{n}_1$. We define *reflection coefficient* $r = E_r/E_i$ and *transmission coefficient* $t = E_t/E_i$ and therefore using (2.35) and (2.38)

$$r = \frac{1-m}{1+m} \tag{2.39}$$

$$t = \frac{2}{1+m} \tag{2.40}$$

Reflectance (R) and *transmittance* T are defined as the ratios of the power flow of the reflected and transmitted waves to that of incident wave and given by

$$R = |r|^2 \tag{2.41}$$

$$T = 1 - R \tag{2.42}$$

Assuming medium 1 is air ($\tilde{n}_1 = 1$) for simplicity and removing the subscripts as they are no longer needed, the reflectance of a material in air or vacuum can be expressed as

$$R = \frac{(n-1)^2 + k^2}{(n+1)^2 + k^2} \tag{2.43}$$

Equation (2.43) states that a material is highly reflective if $n \gg 1$ or $n \ll 1$ or $k \gg 1$.

2.3 Physical Origin of Optical Constants

In **Section 2.1**, we solely concentrated on the case where the medium is nondispersive. However, generally this is not the case. For a dispersive medium, the optical constants are functions of the frequency of the incident field, ω. Therefore, the relationship between $\mathcal{P}$ and $\mathcal{E}$ becomes:

$$\mathcal{P}(\omega) = \epsilon_o \chi(\omega) \mathcal{E}(\omega) \tag{2.44}$$

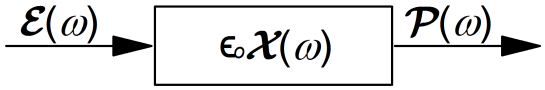

Figure 2.2: Linear system description of a material's response to applied electromagnetic field. Input is the incident electric field, transfer function is defined by the susceptibility. The output is polarization vector.

From a linear system perspective, this equation describes the frequency domain response $\mathcal{P}(\omega)$ of a system with transfer function $H(\omega) = \epsilon_o \chi(\omega)$ to an input $\mathcal{E}(\omega)$. In time domain, the response becomes the convolution of impulse response of the system with the input:

$$\mathcal{P}(t) = \epsilon_o \chi(t) * \mathcal{E}(t) \tag{2.45}$$

$$\mathcal{P}(t) = \epsilon_o \int_{-\infty}^{\infty} \chi(t - t') \mathcal{E}(t') dt' \tag{2.46}$$

Note that the arguments of $\mathcal{P}$ and $\mathcal{E}$ are different (t and t') which means that the response of the system is not instantaneous. Therefore, the response of a material to the incident electric field is not instantaneous. In this section, we investigate the physics behind this phenomenon.

2.3.1 Classical (Lorentzian) Electron Oscillator Model

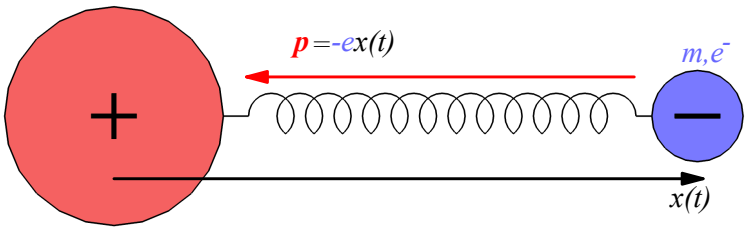

Figure 2.3: Classical electron oscillator model depicts the nucleus (red) and the electron (violet) as two masses connected by a spring.

Lorentzian electron oscillator model handles the field-material relation at a very simple, purely classical yet elegant and accurate way [44]. It depicts the nucleus and the electron as two masses connected to each other by a spring (Figure 2.3). The nucleus is large and immobile compared to the electron. When an external electric field is applied, the electron moves from its equilibrium position by a displacement vector $x(t)$ due to the force ($F_{ext} = e\mathcal{E}(t)$) arising from the interaction between the electric field and the charge of the electron. This is modeled as stretching of the spring (or compression, depending on the direction of the external field). Therefore, there is a restoring force of the spring obeying Hook's law ($F_{spring} = -kx(t)$) where k is the spring constant. In addition, there is a velocity dependent damping force ($F_{damping} = -m\gamma x'(t)$) since the electron will lose energy over time. The sum of these forces gives the net force exerted on the electron and according to Newton's second law:

$$mx''(t) + m\gamma x'(t) + kx(t) = e\mathcal{E}(t) \tag{2.47}$$

where m and e are the mass and charge of electron, respectively and γ is *damping rate*. For a time harmonic electric field $\mathcal{E}(t) = Re\{\mathcal{E}(\omega)e^{jwt}\}$ and $x(t) = Re\{xe^{jwt}\}$, in phasor domain, (2.28) takes the form:

$$-m\omega^2 x + j\omega\gamma mx + \omega_o^2 mx = e\mathcal{E}(\omega) \tag{2.48}$$

where $\omega_o = \sqrt{k/m}$ is the resonance frequency. (2.29) can be solved for x:

$$x = \frac{e\mathcal{E}(\omega)}{m}\frac{1}{\omega_o^2 - \omega^2 + j\omega\gamma} \tag{2.49}$$

Microscopic polarization is defined as $p = ex$:

$$p = \frac{e^2\mathcal{E}(\omega)}{m}\frac{1}{\omega_o^2 - \omega^2 + j\omega\gamma} \tag{2.50}$$

Sum of microscopic polarization for individual electrons in a material where electron concentration is $N(cm^{-3})$ gives the macroscopic polarization, $\mathcal{P}(\omega)$:

$$\mathcal{P}(\omega) = \frac{Ne^2\mathcal{E}(\omega)}{m}\frac{1}{\omega_o^2 - \omega^2 + j\omega\gamma} \tag{2.51}$$

Recalling (2.25) $\mathcal{P}(\omega) = \epsilon_o\chi(\omega)\mathcal{E}(\omega)$, susceptibility can be found:

$$\chi(\omega) = \frac{\omega_p^2}{\omega_o^2 - \omega^2 + j\omega\gamma} \tag{2.52}$$

where ω_p is the plasma frequency of the particular material. Plasma frequency is defined as:

$$\omega_p^2 = \frac{Ne^2}{\epsilon_o m} \tag{2.53}$$

Finally, recalling that dielectric constant ϵ_r and susceptibility are related by (2.11) i.e. $\epsilon_r = 1 + \chi$, we can express dielectric constant as follows:

$$\epsilon_r = 1 + \frac{\omega_p^2}{\omega_o^2 - \omega^2 + j\omega\gamma} \tag{2.54}$$

Real and imaginary parts of dielectric constant can be found according to (2.20):

$$\epsilon_r' = 1 + \frac{\omega_p^2(\omega_o^2 - \omega^2)}{(\omega_o^2 - \omega^2)^2 + \omega^2\gamma^2} \tag{2.55}$$

$$\epsilon_r'' = \frac{\omega_p^2\omega\gamma}{(\omega_o^2 - \omega^2)^2 + \omega^2\gamma^2} \tag{2.56}$$

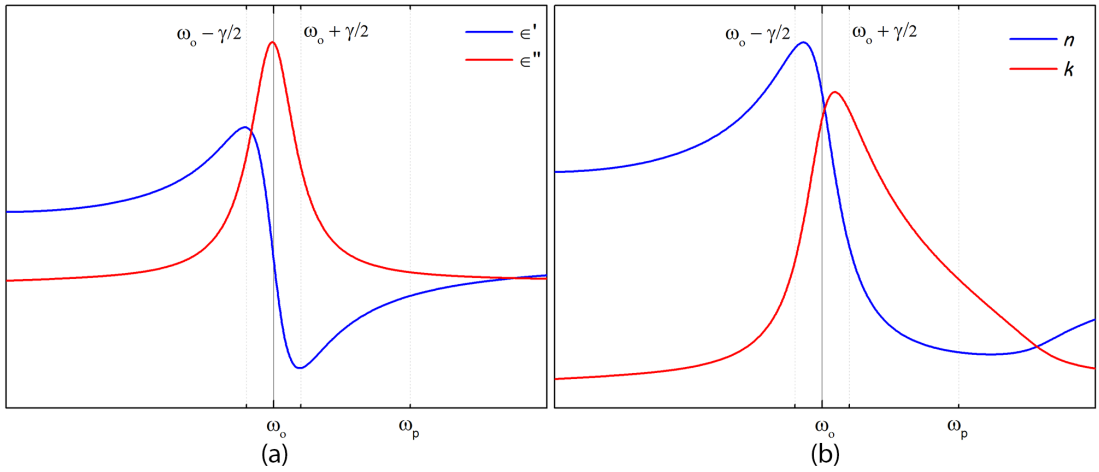

Figure 2.4: (a) Relative dielectric permittivity (b) refractive indices vs frequency according to Lorentzian model

ϵ_r', ϵ_r'', n and k are plotted according to (2.55) and (2.56) on Figure 2.4. There are a few results that could be inferred: as ω increases ϵ' also increases except for $\omega_o - \gamma/2 < \omega < \omega_o + \gamma/2$, which is called the *normal dispersion*. Near resonance, ϵ' reduces with the increasing frequency and this is called the *anomalous dispersion*. Normal and anomalous dispersion is valid for n, as well. γ gives the *full width at half maximum* (FWHM) of the resonance peak of ϵ_r'.

2.3.2 Drude Model

Metals have up to three valence electrons which are not bound to any particular atom. Instead, these electrons are free to roam throughout the metal forming an *electron cloud* [45]. As a consequence of these free flowing electrons, metals are good conductors of both electricity and heat. Also, as there are many available states in the conduction band of metals, electrons can easily absorb low energy photons (visible and infrared) via *intraband absorption* or *free carrier absorption* [44].

The presence of free electrons also determine the optical properties of metals for which the Lorentzian model derived in the previous section is not valid. Instead, χ and ϵ are given by the *Drude model*. As the electrons are *free* i.e. not bound to the nuclei, the amendment to be made in the Lorentzian model is removing the spring. We do this by setting the spring constant $k = 0$ on Equation (2.47).

$$mx''(t) + m\gamma x'(t) = e\mathcal{E}(t) \tag{2.57}$$

Similar to the Lorentzian model, one can easily show that susceptibility is given by the Drude model is:

$$\chi(\omega) = -\frac{\omega_p^2}{\omega^2 - j\omega\gamma} \tag{2.58}$$

Therefore, dielectric function is given by:

$$\epsilon_r = 1 - \frac{\omega_p^2}{\omega^2 - j\omega\gamma} \tag{2.59}$$

The imaginary and real parts of dielectric constant can be found as:

$$\epsilon_r' = 1 - \frac{\omega_p^2}{\omega^2 + \gamma^2} \tag{2.60}$$

$$\epsilon_r'' = \frac{\omega_p^2\gamma}{\omega(\omega^2 + \gamma^2)} \tag{2.61}$$

The plasma frequency and the damping ratio of some metals are given in Table 2.1 below [46, 47]. Note that the plasma frequency is given as the ordinary frequency in Hz, not the radial frequency (rad/s).

Table 2.1: The plasma frequency and the damping ratio of some metals

Metal	Plasma frequency (THz)	Damping ratio (Thz)
Au	2183	6.46
Ag	2180	4.35
Pt	1244	16.73
Al	3570	19.79
Cu	1914	8.34
Na	1381	6.67
K	889.6	4.45

ϵ_r', ϵ_r'', n and k are plotted according to (2.60) and (2.61) on Figure 2.5.

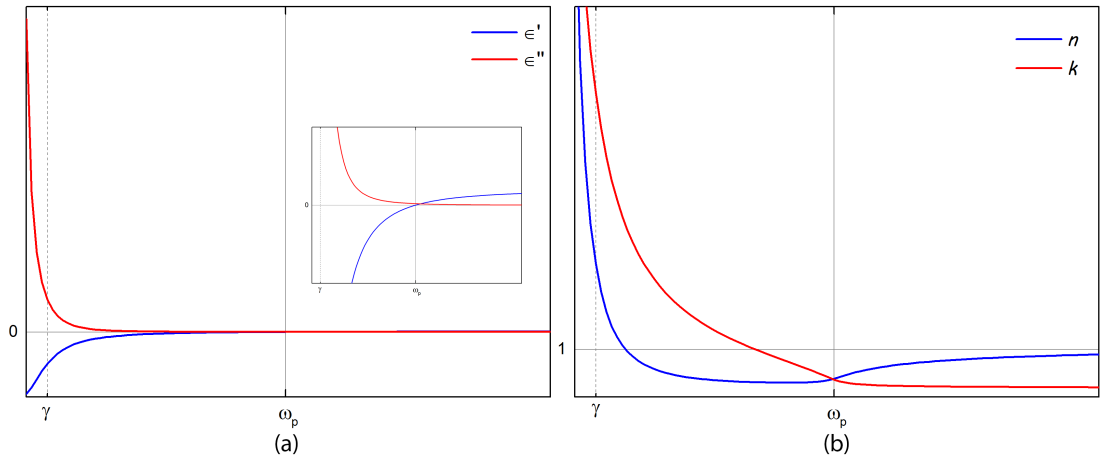

Figure 2.5: (a) Relative dielectric permittivity, inset is the zoomed version i.e. y axis is rescaled (b) refractive indices vs frequency according to Drude model

At frequencies much lower than the damping ratio and the plasma frequency, i.e. $\omega \ll \gamma, \omega \ll \omega_p$; ϵ_r' is negative and $\epsilon_r'' \gg \epsilon_r'$ in terms of magnitude. Also, $n \gg 1$ and $k \gg 1$. Recalling the result found in Section 2.2, i.e. a material is highly reflective if $n \gg 1$ or $n \ll 1$ or $k \gg 1$; we can state that metals are highly reflective at low frequencies. At these frequencies, metals are very conductive.

For $\omega \gg \gamma$, (2.60) can be simplified as

$$\epsilon_r' = 1 - \frac{\omega_p^2}{\omega^2} \tag{2.62}$$

Therefore we can simply state that at the plasma frequency $\epsilon_r' = 0$. Indeed, the inset of Figure 2.5(a) confirms this.

When $\omega \gg \gamma$ and $\omega < \omega_p$; ϵ_r' is again negative but $\epsilon_r' \gg \epsilon_r''$ in terms of magnitude. Therefore we can state that the dielectric function is practically real. Figure 2.5(b) shows that, at such frequencies $n \ll 1$ therefore the material is again reflective.

When $\omega > \omega_p$, ϵ_r' becomes positive, ϵ_r'' and k are approaching 0. Therefore, at these frequencies, metals become transparent and allows the transmittance of electromagnetic field through.

Although some metals like Na and K are well modeled using the Drude model

as they are dominated by the free electrons; for most metals including Au and Ag the contribution of bound electrons is not negligible [48]. To represent such dielectricity of these metals, Drude model is extended by adding an extra dielectric constant named the *background permittivity*, ϵ_∞.

$$\epsilon_r = \epsilon_\infty - \frac{\omega_p^2}{\omega^2 + \gamma^2} - j\frac{\omega_p^2 \gamma}{\omega(\omega^2 + \gamma^2)} \tag{2.63}$$

2.3.3 Multi-oscillator Lorentz-Drude Model

For many materials, there are more than one resonance condition such as electron-nucleus vibration, molecular vibration (symmetic stretching, asymmetric stretching etc). Nevertheless, all of these phenomena can be modeled using the Lorentzian and the Drude oscillators. In such a case, the dielectric function of the material is given by the superposition of the individual resonances at different frequencies.

$$\epsilon_r = \epsilon_\infty - \frac{\omega_{p,0}^2}{\omega^2 - j\omega\gamma_0} + \sum_{i=1}^{i_{max}} \frac{\omega_{p,i}^2}{\omega_{o,i}^2 - \omega^2 + j\omega\gamma_i} \tag{2.64}$$

Subscripts denote different oscillators. Note that, 0^{th} order oscillator is the Drude oscillator.

2.4 Surface Plasmons

Surface plasmons are electromagnetic excitations confined to the interface between a dielectric and a conductor [49]. The field is evanescent in the perpendicular direction and propagates at the interface. Wood was the first to observe this phenomenon while he was working on metallic diffraction gratings [2]. In this section, first the surface plasmons are derived starting from the wave equation. Then, the excitation of surface plasmons via grating coupling is discussed.

2.4.1 Derivation of Surface Plasmon Equations

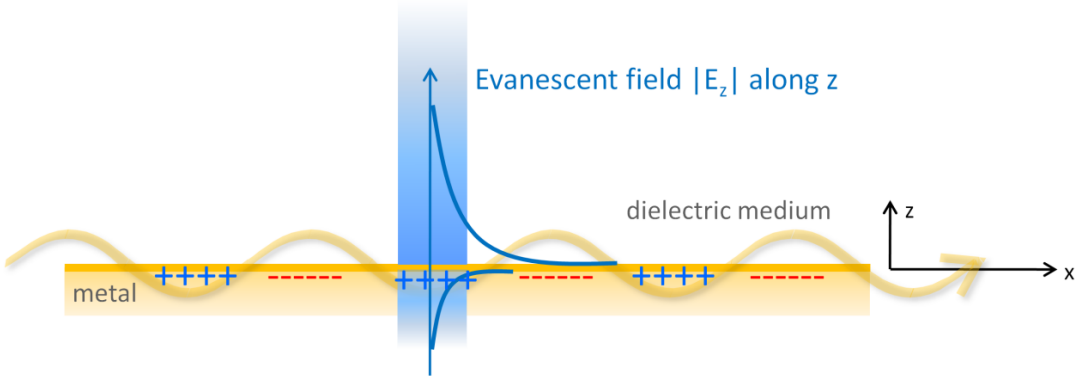

Figure 2.6: The propagation geometry for surface plasmon. It propagates along the interface but evanescent in the z direction.

As stated before, surface plasmons are electromagnetic waves propagating at the dielectric/metal interface. Therefore, we seek solutions to the wave equation (2.16) for the geometry given in Figure 2.6 (adapted from [50]). The field propagates in x direction along the interface which is at $z = 0$. For $z < 0$, the medium is the metal with relative permittivity ϵ_m and for $z > 0$, the medium is dielectric (ϵ_d).

For a time-harmonic wave ($\frac{\partial}{\partial t} = j\omega$) propagating in x direction with wavevector β ($\frac{\partial}{\partial x} = -j\beta$) and constant in y direction ($\frac{\partial}{\partial y} = 0$), the curl equations i.e. (2.3) and (2.4) reduces to two sets of equations:

$$\frac{\partial E_x}{\partial z} + j\beta E_z = -j\omega\mu_o H_y \tag{2.65}$$

$$E_x = j\frac{1}{\omega\epsilon}\frac{\partial H_y}{\partial z} \tag{2.66}$$

$$E_z = -\frac{\beta}{\omega\epsilon}H_y \tag{2.67}$$

$$\frac{\partial H_x}{\partial z} + j\beta H_z = j\omega\epsilon E_y \tag{2.68}$$

$$H_x = -j\frac{1}{\omega\mu_o}\frac{\partial E_y}{\partial z} \tag{2.69}$$

$$H_z = \frac{\beta}{\omega \mu_o} E_y \tag{2.70}$$

The mode defined by (2.65) to (2.67) is called the *transverse magnetic* or *TM* polarization. Equations (2.68) to (2.70) defines the *transverse electric* (*TM*) polarization. However, TE polarization does not satisfy the boundary conditions at the metal/dielectric interface [49]. Therefore, surface plasmons only exist for TM polarization and this is demonstrated below:

The wave equation for TM mode can be derived by substituting (2.66) and (2.67) in (2.65):

$$\frac{\partial^2 H_y}{\partial z^2} + (k_o^2 \epsilon - \beta^2 H_y) = 0 \tag{2.71}$$

where k_o is the wavevector in vacuum.

Since the wave is propagating in the x drection and evanescent in the z direction, inside the dielectric ($z > 0$), we can define H_y as

$$H_y = e^{-j\beta x} e^{-k_d z} \tag{2.72}$$

where k_d is the wavevector in the z direction inside the dielectric. Therefore, inserting permittivity ϵ_d of the dielectric into (2.66) and (2.67), the electric field components in the dielectric can be written as

$$E_x = -j \frac{1}{\omega \epsilon_d} k_d e^{-j\beta x} e^{-k_d z} \tag{2.73}$$

$$E_z = -\frac{\beta}{\omega \epsilon_d} e^{-j\beta x} e^{-k_d z} \tag{2.74}$$

The boundary conditions require that the tangential components of magnetic field should be equal on both sides of the interface. Therefore, inside the metal (i.e. $z < 0$), H_y can be defined as

$$H_y = e^{-j\beta x} e^{k_m z} \tag{2.75}$$

where k_m is the wavevector in the z direction inside the metal. Note that the sign before the wavevector has changed, compared to (2.72). This is required for the

evanescent wave nature since inside the metal $z < 0$.The electric field components inside the metal (ϵ_m) are

$$E_x = j\frac{1}{\omega\epsilon_m}k_m e^{-j\beta x}e^{k_m z} \tag{2.76}$$

$$E_z = -\frac{\beta}{\omega\epsilon_m}e^{-j\beta x}e^{k_m z} \tag{2.77}$$

The boundary conditions also require that the tangential components of electric field (E_x) should be equal on both sides of the interface. Therefore, for $z = 0$, (2.73) and (2.76) should be equal. This results in

$$\frac{k_d}{k_m} = -\frac{\epsilon_d}{\epsilon_m} \tag{2.78}$$

Note that, for this equation to be satisfied, one of the dielectric constants should be negative. Therefore, in the quest for searching alternative plasmonic materials, one should seek materials with negative dielectric constants.

Inserting (2.72) and (2.75) into the wave equation i.e. (2.71) yields

$$k_d^2 + k_o^2\epsilon_d - \beta^2 = 0 \tag{2.79}$$

$$k_m^2 + k_o^2\epsilon_m - \beta^2 = 0 \tag{2.80}$$

Combining these two equations and (2.78), the dispersion relation for surface plasmons propagating at the interface between a metal and dielectric is found:

$$\beta = k_o\sqrt{\frac{\epsilon_d\epsilon_m}{\epsilon_d + \epsilon_m}} \tag{2.81}$$

Plasmon dispersion relation at a planar metal/dielectric interface is given on Figure 2.7. The part of the plasmon dispersion line that is to the right of the light line gives the surface plasmon polariton modes. The part above the plasma frequency gives the bulk plasmons i.e. fields propagating in metal. The transition between is caused by the damping.

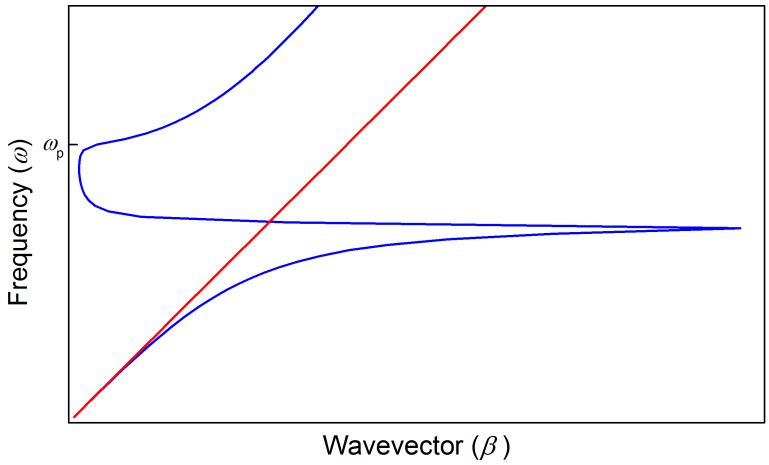

Figure 2.7: Plasmon dispersion relation at a metal/dielectric interface (blue line). The red line is the so called light line. The part of the plasmon dispersion line that is to the right of the light line gives the surface plasmon polariton modes. The part above the plasma frequency gives the bulk plasmons i.e. fields propagating in metal. The transition between is caused by the damping.

2.4.2 Excitation of Surface Plasmons

As seen on Figure 2.6, surface plasmon modes have larger wavevector than the incident light (light line) in the medium. In quantum theory, the wavevector of light is related to the momentum of the photons ($p = \hbar k$). Therefore one can state that the momentum of incident light is not enough to excite surface plasmons and it is impossible to generate surface plasmons by directly applying electromagnetic field to a planar interface.

Nevertheless, there are several methods for exciting surface plasmons including very common Kretschman prism coupling [51], grating coupling and impact coupling etc [49]. However, here only grating coupling will be discussed as this is the method that is used in this study. There is a very good discussion of other methods in [49].

When the surface of the metal is periodically corrugated as in Figure 2.8, the incident radiation will scatter from the gratings and the x component of its wavevector will be increasing or decreasing by integer multiples of the wavevector of the grating structure. If the wavevector of one of such mode is higher than that

of the incident light, surface plasmons can be excited as the wavevector mismatch can be overcome.

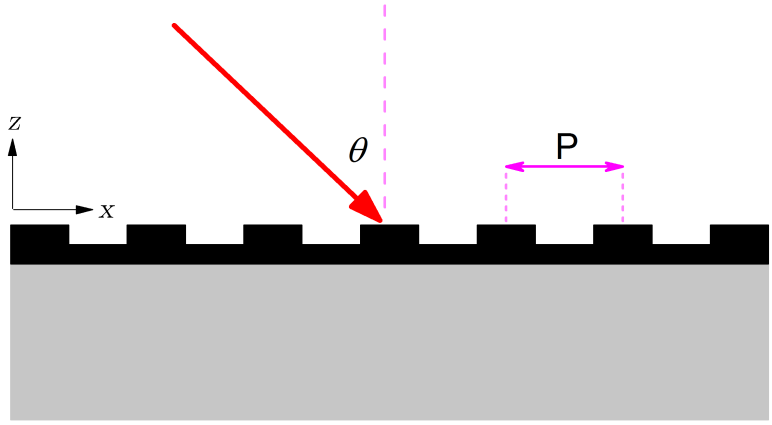

Figure 2.8: Periodic grating geometry used to generate surface plasmons. The red line represents the incident radiation, making an angle θ with the normal. The period (P) is defined as the center to center distance of the gratings.

The x component of the wavevector of the incident radiation is $k_x = ksin\theta$. The wavevector of the grating structure is defined as $G = \frac{2\pi}{P}$ where P is the period. Therefore, the phase matching condition is given by the following equation:

$$\beta = ksin\theta + mG \tag{2.82}$$

where β is the surface plasmon wavevector and m is any integer.

For normal incidence, $\theta = 0$ and for first order resonance, $m = 1$. Using the plasmon dispersion equation (2.81) and substituting $\lambda = \frac{2\pi}{k}$, first order resonance wavelength for normal incidence can be found:

$$\lambda = P\sqrt{\frac{\epsilon_d \epsilon_m}{\epsilon_d + \epsilon_m}} \tag{2.83}$$

2.4.3 Plasmonic Figures of Merit

There are two important figures of merit (FOM) regarding the performance of plasmonic materials in terms of performance for various applications: *Mode confinement width* (D_W) and *propagation length* (L_P).

Free electron damping and interband transitions in metals results in complex dielectric constants where the imaginary part is nonzero. This corresponds to loss (absorption) in metals. Therefore, while propagating surface plasmons are damped with the propagation length, $L_P = 1/Im\{\beta\}$. Inserting the dispersion equation (2.81) into (2.84) yields

$$L_P = 1 \Big/ Im\left\{ k_o \sqrt{\frac{\epsilon_d \epsilon_m}{\epsilon_d + \epsilon_m}} \right\} \tag{2.84}$$

For most metals, propagation length is between 10 and 100 μm in the visible wavelengths [49].

Due to the evanescent nature of the surface plasmons, field is confined in the perpendicular direction. Plasmonics allow the confinement of electric field into volumes smaller than the diffraction limit. This high confinement results in enhancement of field which is why plasmonics is preferred for most applications. The decay length into the metal is $\delta_m = 1/k_m$ and into the dielectric it is $\delta_d = 1/k_d$ where k_m and k_d are wavevectors of the suface plasmon in the perpendicular (z) direction in metal and the dielectric, respectively. Wavevectors in the perpendicular direction are $k_z = \sqrt{\beta^2 - \epsilon k_o^2}$. Therefore, the decay lengths can be found as

$$\delta_m = 1 \Big/ Re\left\{ k_o \sqrt{\frac{-\epsilon_m^2}{\epsilon_d + \epsilon_m}} \right\} \tag{2.85}$$

$$\delta_d = 1 \Big/ Re\left\{ k_o \sqrt{\frac{-\epsilon_d^2}{\epsilon_d + \epsilon_m}} \right\} \tag{2.86}$$

For plasmonic waveguiding applications, confinement width is expressed by the following equation [52]:

$$D_W = \begin{cases} \delta_{air} & |\epsilon_m| \geq e \\ \delta_{air} + \delta_m(1 - \ln(|\epsilon_m|)) & |\epsilon_m| < e \end{cases} \tag{2.87}$$

In surface plasmon waveguides, there is a trade-off between the propagation length and the confinement width. The better the confinement, the shorter the propagation length. While choosing a material (i.e. a metal or an alternative plasmonic material), one should balance this trade-off.

Chapter 3

ALD Grown ZnO as a Plasmonic Material

ZnO is a II-VI compound with a substantial ionic character which results in a high bandgap energy of 3.37 eV (368 nm). Although it can assume wurtzite, zinc-blende and rocksalt crystal structures, under ambient conditions the thermodynamically stable phase is the wurtzite symmetry. Applications of ZnO in electronics and photonics include LEDs, lasers, photodiodes, solar cells, field effect transistors and piezoelectric devices [53].

In this chapter, atomic layer deposition (ALD) growth and optical characterization of ZnO is presented. Also, plasmonic properties of ZnO are discussed.

3.1 Growth

ALD is a monolayer level deposition technique which is based on sequential exposure of reactants called the precursors. As it depends on surface reactions, growth at the surface is self limiting which increases the uniformity and conformality of the grown layers.

There are 4 steps forming each cyle of ALD growth: (i) exposure of first precursor and reactions at the surface reactive sites, (ii) purging in order to remove excess precursors and by-products, (iii) exposure of the second precursor and reactions (iv) purging to remove excess precursors and by-products. This is called one cycle and growth of a film at desired thickness can be achieved after N cycles.

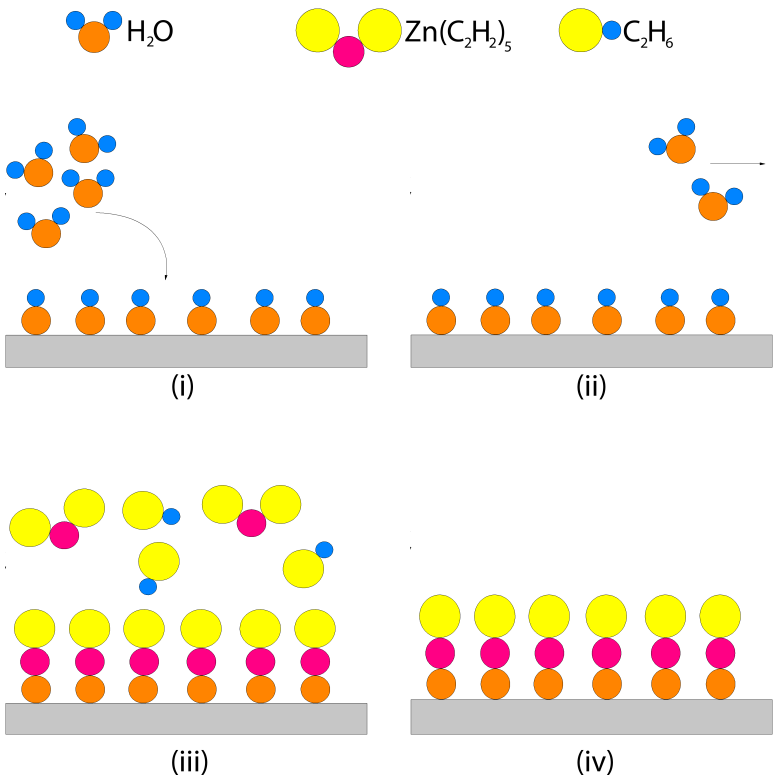

Figure 3.1: Steps of the ALD cycles of ZnO growth: (i) Exposure of H_2O and reactions at the surface (ii) Purging in order to remove excess water and by-products, (iii) Exposure of *Diethyl Zinc* (DEZ) and reactions (iv) Purging to remove excess precursors and by-products.

ALD growth of ZnO films are carried out using Cambridge Savannah 100 Thermal ALD system at UNAM Cleanroom Facility. The precursors are diethylzinc (DEZ) and milli-Q water (H_2O) and the substrate is n-type (100) Si wafer. The growth is conducted at temperatures of 120°C, 200°C and 250°C for 300 cycles.

The chemical reactions governing the ALD growth of ZnO are as follows [54]: in the DEZ phase, i.e. when DEZ is exposed:

$$surface - O - H + Zn(C_2H_5)_2 \rightarrow surface - O - H - Zn - C_2H_5 + C_2H_6$$

After this step, excess DEZ and C_2H_6 is removed by purging. In the H_2O phase;

$$surface - O - H - Zn - C_2H_5 + H_2O \rightarrow surface - O - H - Zn - O - H + C_2H_6$$

Excess H_2O and C_2H_6 is removed by purging. The growth continues by repeating these steps.

3.2 Optical Characterization

Optical characterization of grown films is conducted using spectroscopic ellipsometry technique.

3.2.1 Spectroscopic Ellipsometry Technique

Ellipsometry is a technique that is used to extract the optical constants of a film by measuring the change in the polarization of a light beam reflected from the film.

The polarization of light is determined by the route the direction of electric field follows over time. The electric field can be written in terms of two components, one is parallel and the other is perpendicular to the plane of incidence and they are called the p and s polarization, respectively (Figure 3.2).

If the two components are in phase, the light is *linearly polarized*. If there is a phase difference of $\pi/2$ and the amplitudes of the two components are equal, the light is *circularly polarized*. Except these two extreme conditions, the electric field of the wave draws an ellipse over time (The name ellipsometer derives from here.).

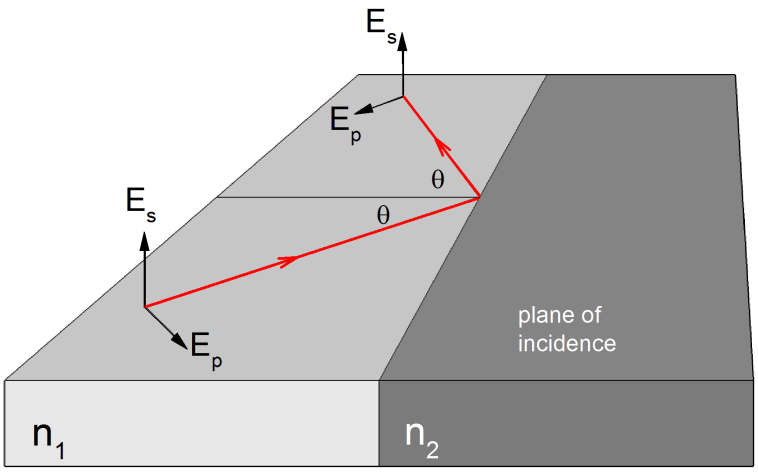

Figure 3.2: Reflection at the boundary of two different media. If the electric field is perpendicular to the plane of incidence, it is called the s polarization. If it is parallel, the light is p polarized.

In Section 2.2, reflection coefficient at a boundary for normal incidence was derived. For normal incidence, the polarization of light does not affect the reflection coefficient. However, when the angle of incidence is nonzero, s and p polarized components reflect with different reflection coefficients. These coefficients are given by the *Fresnel equations*:

$$r_s = \frac{n_1 cos\theta_1 - n_2 cos\theta_2}{n_1 cos\theta_1 + n_2 cos\theta_2} \tag{3.1}$$

for s polarized light and

$$r_p = \frac{n_2 cos\theta_1 - n_1 cos\theta_2}{n_2 cos\theta_1 + n_1 cos\theta_2} \tag{3.2}$$

for p polarization.

An ellipsometer system (Figure 3.3) uses a light source and a polarizer to generate the incident beam [55]. The linearly polarized light is reflected from the surface and its polarization after reflection is determined by the *rotating analyzer*. By comparing the polarization states of the incident and the reflected beam, what ellipsometer measures (ρ) is the ratio of r_p/r_s. It can we written in terms of two angular variables, Δ and Ψ.

$$\rho = \frac{r_p}{r_s} = tan(\Psi)e^{i\Delta} \tag{3.3}$$

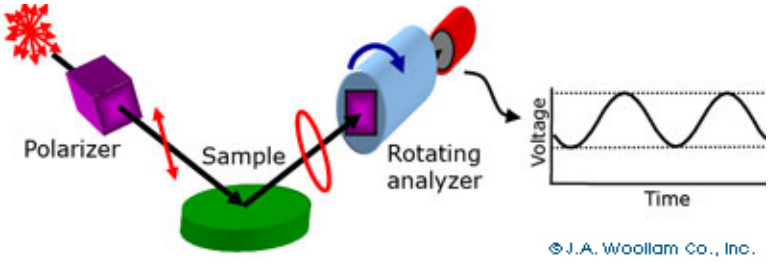

Figure 3.3: A basic scheme for an ellipsometer system. The randomly polarized light generated by the light source is linearly polarized by the polarizer and the incident beam is formed. After reflection, the polarization of the reflected beam is determined by the rotating analyzer and the detector.

In spectroscopic ellipsometry, data analysis is conducted by a software by fitting theoretical models to the measurement result. The theoretical model can consist of multi-oscillator Lorentz-Drude model (as described in Section 2.3.3) in the absorptive wavelength ranges. The transparent wavelength ranges are modelled by the *Cauchy dispersion equation* [56].

When thin films are characterized by ellipsometry, multiple reflections at the air/film and film/substrate interfaces causes an infinite series (Figure 3.4). In this case, the thickness of the film becomes a fit parameter to be determined along with the optical constants.

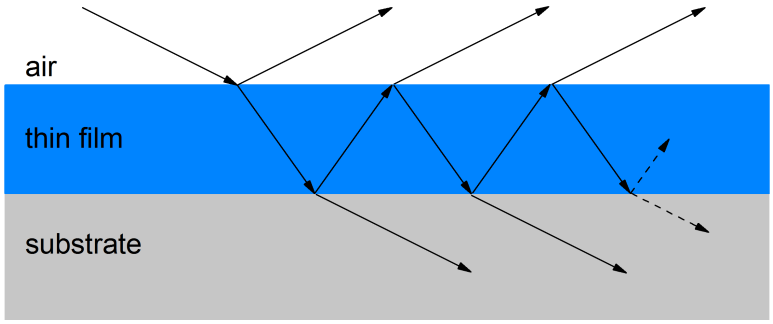

Figure 3.4: Multiple reflections at an air/thin film/substrate structure causes an infinite sum of the reflected components

3.2.2 Optical Properties of ZnO

Optical characterization of grown films is conducted using J.A. Woollam V-Vase (0.4-1.7 μm) and IR-Vase (1.8-15 μm) ellipsometers. In order to minimize fit errors, the measurements are conducted at two different angles of incidence, 57° and 67°.

The bandgap of ZnO corresponds to 368 nm. ZnO films are transparent from this point up to the near infrared [57]. Hence, the measurements taken with V-Vase (0.4-1.7 μm) are modelled with the Cauchy dispersion equation:

$$n(\lambda) = A + \frac{B}{\lambda^2} + \frac{C}{\lambda^4} \tag{3.4}$$

$$k(\lambda) = A_k e^{E_k\left(\frac{hc}{\lambda} - E_g\right)} \tag{3.5}$$

where A, B, C, A_k and E_k are fit parameters and E_g is the band gap energy (3.37 eV). The fit parameters used for the ZnO films are given on Table 3.1.

Table 3.1: Caucy dispersion model fit parameters used for the optical characterization of ZnO films in the 0.4-1.7 μm range

Growth Temp.	Thick. (nm)	A	B	C	A_k	E_k (eV^{-1})
120 °C	45.47	1.816	5.05×10^{-2}	3.920×10^{-4}	4.685×10^{-2}	0.999
200 °C	44.86	1.813	4.74×10^{-2}	2.836×10^{-4}	2.821×10^{-2}	0.2
250 °C	34.62	1.786	3.03×10^{-2}	2.844×10^{-5}	2.175×10^{-2}	0.229

The measurements taken with IR-Vase (1.8-15 μm) are modelled with the multi-oscillator Drude-Lorentz model described in Section 2.3.3 since absorption of light by the films are not negligible anymore due to the existence of free carriers. Equation (2.64) can be rewritten for $i = 1$ as follows:

$$\epsilon(\omega) = \epsilon_\infty - A_0 \frac{\Gamma_0}{(\hbar\omega)^2 + j\Gamma_0\hbar\omega} + A_1 \frac{\Gamma_1\hbar\omega_o}{(\hbar\omega_o)^2 - (\hbar\omega)^2 - j\Gamma_1\hbar\omega} \tag{3.6}$$

Note that the term with subscript 0 arises from the Drude oscillator and the one with subscript 1 arises from the Lorentz oscillator. $\hbar$ is the reduced Planck constant, A_0 and A_1 are the amplitudes of the oscillators, Γ_0 and Γ_1 are broadening and ω_o is the resonance frequency of the Lorentz oscillator.

The fit parameters of the multi-oscillator Drude-Lorentz model used for ZnO films are given on Table 3.2. Note that, this time the film thickness is not a fit parameter as it is found in the previous measurement and entered to the software.

Table 3.2: Multi-oscillator Drude-Lorentz model fit parameters used for the optical characterization of ZnO films in the 1.8-15 μm range

Growth Temp. (°C)	ϵ_∞	A_0	Γ_0	A_1	Γ_1	ω_0
120	3.71	51.20	48.30	1694	8468	397.3
200	3.65	51.59	52.74	8109	2024	397.0
250	3.25	55.77	60.98	14886	2241	396.5

The measured optical constants of the ZnO films are given on Figure 3.5.

3.3 Plasmonic Properties of ZnO

As seen on Figure 3.5 (a), the real part of the relative permittivities (ϵ') are given. For ZnO film grown at 200 °C, $\epsilon' < 0$ for $\lambda > 8\ \mu m$ and for the film grown at 250 °C, $\epsilon' < 0$ for $\lambda > 4.08\ \mu m$. Therefore, these two films show metallic properties for these wavelengths and can be used for plasmonic applications.

Using the plasma wavelengths mentioned above, the plasma frequencies can be calculated as 2.35×10^{14} and 4.62×10^{14} rad/s, respectively. Using the equation given in (2.53) and inserting the effective electron mass in ZnO as $m = 0.23 m_o$ where m_o is the electron mass [58]; carrier densities can be calculated as $4.056 \times 10^{18}\ cm^{-3}$ and $1.542 \times 10^{19}\ cm^{-3}$. The increase in the carrier density with increasing growth temperature is due to the increased oxygen vacancies which acts as n type doping in ZnO. Finally, these numbers are sufficiently close to the reported values in the literature [54]. The slight difference can be attributed to different growth conditions.

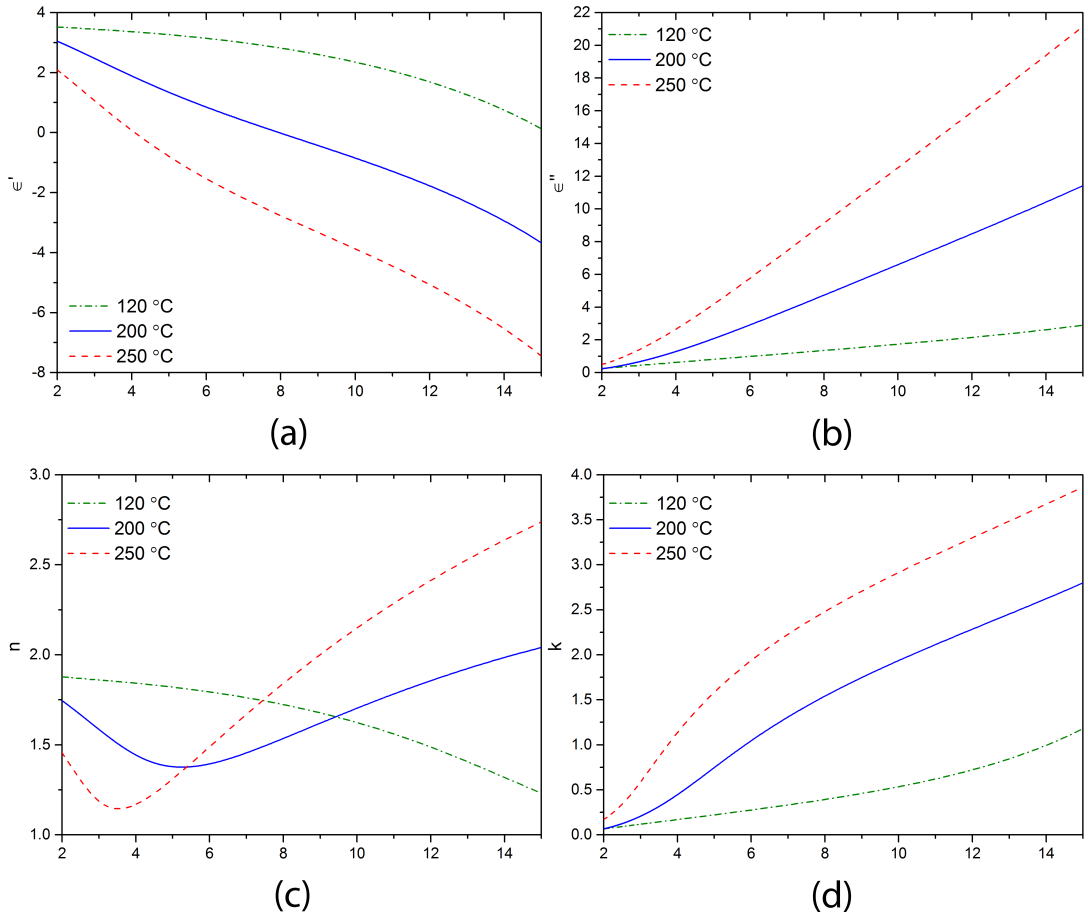

Figure 3.5: Optical constants of ZnO layers grown at different temperatures. In all plots, the x axis is the wavelength (μm). (a) Real and (b) Imaginary part of the relative permittivity. (c) Real and (d) Imaginary part of the complex refractive index.

In Figure 3.6, permittivity of ZnO and Au are given for comparison [59]. It can be seen that $\epsilon'_{ZnO} \ll \epsilon'_{Au}$ and $\epsilon''_{ZnO} \ll \epsilon''_{Au}$. Therefore, one can state that optical loss is much lower in ZnO compared to gold.

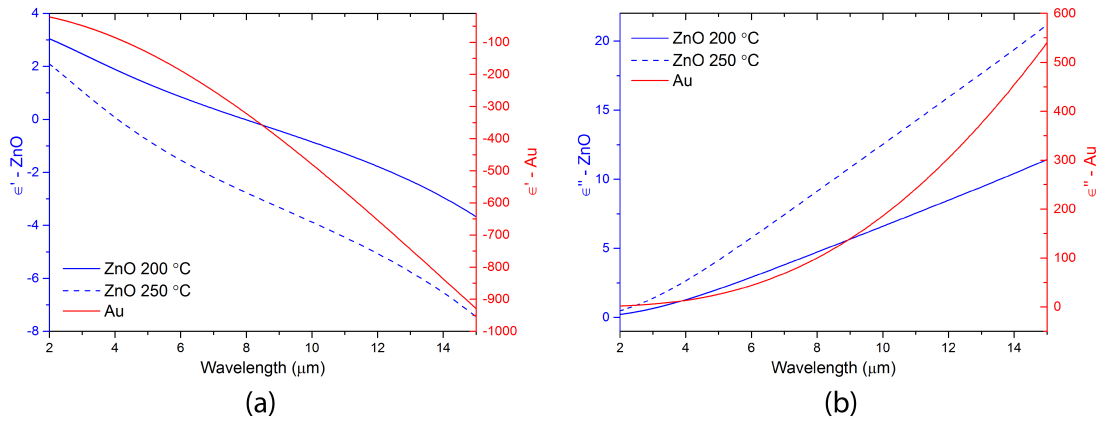

Figure 3.6: a) Real and b) Imaginary parts of permittivity of ZnO and Au for comparison. The left axis is the permittivity of ZnO (blue lines) and the right axis is the permittivity of gold (red lines).

Plasmonic figures of merit (FOM) such as *confinement width* (D_W) and *propagation length* (L_P) were given in Section 2.4.3. Here, these FOM are calculated both for ZnO and Au and given on Figure 3.7. It is seen that gold enjoys a longer propagation length. Since the real permittivity of gold is much larger than that of ZnO as shown on Figure 3.6 a), electromagnetic field penetrates less into gold compared to ZnO. This results in more absorption in ZnO and a shorter propagation length compared to gold. Therefore, gold is more advantageous when a longer propagation length is needed, such as in waveguiding applications.

On the other hand, ZnO films allow a better confinement of the field. Better confinement leads to higher enhancement of the electromagnetic fields. A higher field enhancement is desirable in localized surface plasmon applications such as biosensors. Therefore, ZnO is superior to gold in this kind of applications.

There is a trade-off between the propagation length and the confinement width. As mentioned before, while choosing a material (i.e. a metal or an alternative plasmonic material), one should balance this trade-off. Since the optical parameters can be easily tuned by changing the growth temperature, ZnO gives a higher degree of freedom by offering control of the parameters that determine the figure of merit and allow their effective optimization.

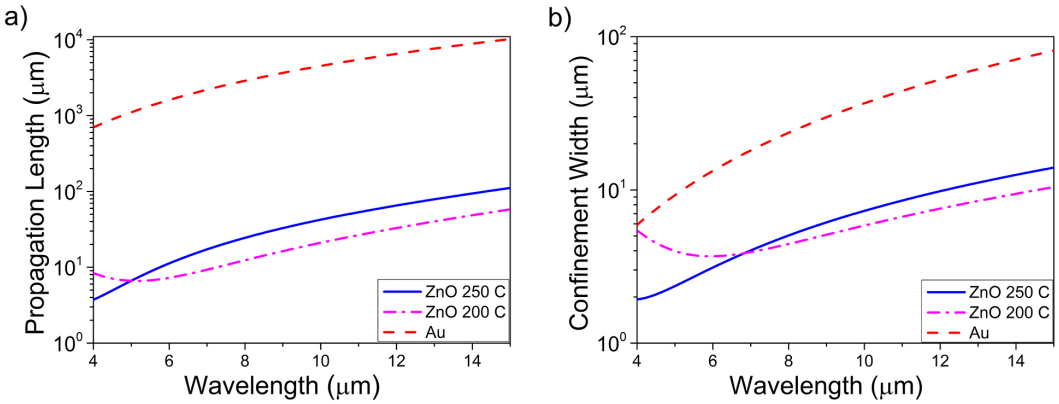

Figure 3.7: Comparison of Au and ZnO grown at 200 °C and 250 °C in terms of a) surface plasmon propagation length and b) mode confinement width at the air interface. Gold offers higher propagation length, yet ZnO provides higher confinement of the electromagnetic field. Also, ZnO allows to fine tune these figures as there is a small difference between the performances of ZnO grown at 200 °C and 250 °C.

In the end, we can state that ZnO is a promising alternative plasmonic material.

Chapter 4

Applications of ALD Grown ZnO

Computational simulations are the cheapest experimental setup in terms of cost and time. Therefore, in photonic applications, making simulations is desirable before fabricating devices. First presented by Kane Yee in 1966 [60], FDTD method is able to simulate a variety of electromagnetic problems which include inhomogeneous, dispersive, and anisotropic media with applications ranging from scattering to antenna simulation [61]. It solves the Maxwell's equations by approximating the partial derivatives using discrete difference equations (thus finite-difference). The problem is discretized both in time and space. The simulation scheme is divided into a grid and at each time step, electric and magnetic field components are calculated by using the values found in the previous step. Therefore, the fields propagate along the simulation scheme and evolve in time (thus time-domain). Although this algorithm requires intensive computation power, it is not a problem with today's fast computers available at affordable prices.

To conduct the FDTD method, a commercial software package named *FDTD Solutions* by *Lumerical Inc* is used [62]. It has a user-friendly interface, intuitive scripting language and it is well acknowledged by the scientific community [63,64].

In this chapter, two different applications of ALD grown ZnO are computationally demonstrated: An ultra-wide-band absorber and a new generation microbolometer.

4.1 Ultra-Wide-Band Infrared Absorber with ZnO Plasmonic Gratings

In Chapter 3, it is shown that ALD grown ZnO can be used as a plasmonic material in the infrared. To demonstrate plasmonic resonances in ZnO, an infrared absorber with ZnO grating structure is designed (Figure 4.1 a,b). The parameters defining the structure are width (w), height (h) and period (P) of the gratings. Si is chosen as substrate since it is common. Also, for comparison, a reference simulation setup is formed where a slab of ZnO which does not utilize gratings is placed on Si substrate (Figure 4.1 c,d).

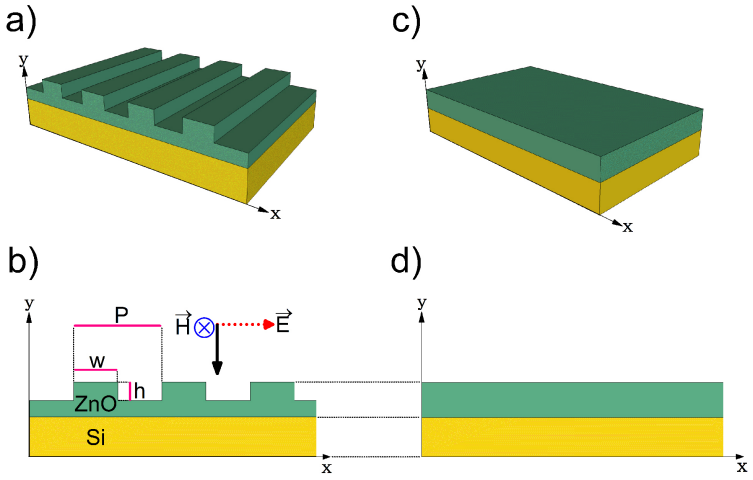

Figure 4.1: Simulated structures: Plasmonic grating structure, a) 3D and b) 2D side view. TM polarized EM wave has electric field along x axis. Reference structure, c) 3D and d) 2D side view. Note that, the thickness of ZnO film is the same for the reference and the grating structure.

A 2-D simulation setup is configured with the periodic boundary conditions on the x axis and *perfectly matched layers* (PML) on the y axis (Figure 4.2). The periodic boundary condition make the grating appear as an infinite array along the x axis. The PML boundary condition works by artificially adding lossy terms such that the impedance going from the background medium to the PML is intact. Therefore, there is no reflection. Using PML boundary immediately after Si causes the substrate to be infinite in extend. The mesh grid around and inside ZnO region is set such that the mesh steps in x and y directions are 25 nm.

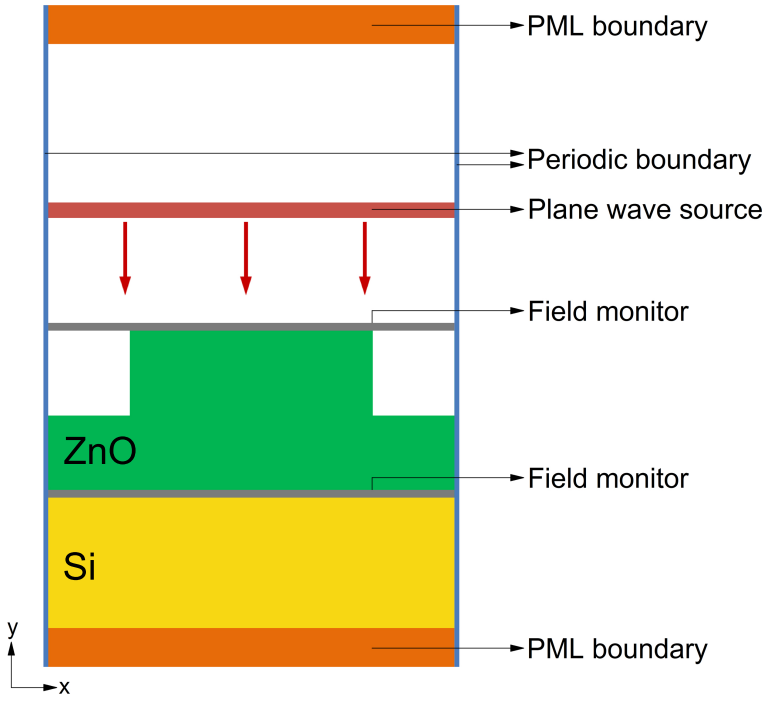

Figure 4.2: Simulation setup used for the ZnO grating structure.

The structure is illuminated with a plane wave source where the wavelength range of the light is 4-15 μm. Also, the plane wave is TM polarized, i.e. the electric field is along the x axis, which enables the generation of surface plasmons in the grating structure. Si substrate is modelled with a constant refractive index n = 3.42 and extinction coefficient k = 0, within the wavelength range of interest. The ZnO film is modelled using the optical parameters of ZnO grown at 250 °C.

In order to investigate resonant conditions, absorption in the ZnO film is calculated using the difference of power transmission through two field monitors, one located on top of gratings and another at the ZnO/Si interface ($y = 0$). The power transmission through the top monitor is $P_1 = 1 - R$, where 1 denotes the incident light and R is the reflection from the grating structure. The transmission through the monitor at $y = 0$ is $P_2 = T$ where T is the power transmitted through the ZnO film. The absorbed power (A) can be calculated using $A = 1 - R - T$ which equals $A = P_1 - P_2$.

For demonstration purpose, the period is chosen $P = 5\ \mu m$, width of the

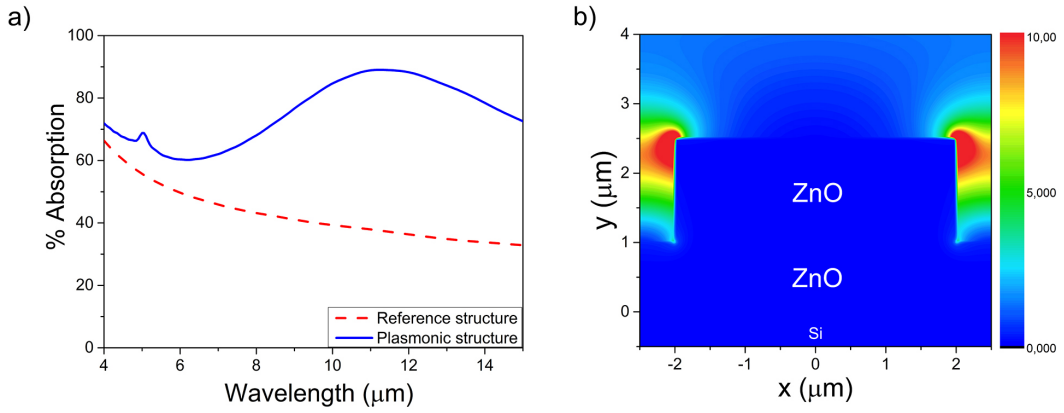

Figure 4.3: a) Comparison of the absorption spectra of the reference structure and the plasmonic structure. b) Electric field intensity profile around the gratings ($\lambda = 11.5\ \mu m$).

grating is chosen as $w = 4\ \mu m$ and the grating height is $h = 1.5\ \mu m$. The base thickness of ZnO is chosen as $1\ \mu m$, in order to de-couple the resonances in the gratings from the effects of the substrate, as we are aiming to generate plasmons at the air/ZnO interface.

The absorption spectra for both the reference and the plasmonic structure are given on Figure 4.3. A resonance peak is observed at a wavelength that is very close to the grating periodicity of $5\ \mu m$. This resonance can be attributed to the excitation of surface plasmon polaritons. In Section 2.4.2, it was shown that first order resonance wavelength in plasmonic grating structure is

$$\lambda = P\sqrt{\frac{\epsilon_d \epsilon_m}{\epsilon_d + \epsilon_m}} \tag{4.1}$$

When the dielectric is air, $\epsilon_d = 1$. When $\epsilon_m \gg 1$, the equation (4.1) reduces to $\lambda \approx P$ (for ZnO, $\epsilon_m = -0.797 + j4.162$ at $\lambda = P = 5\ \mu m$).

In addition, a stronger broadband resonance is observed at $\lambda = 11.5\ \mu m$. Since the separation between the gratings are much lower than the grating width, the structure can be treated as a truncated MDM slot waveguide and supports a fundamental edge mode [65, 66]. In Figure 4.3b, the intensity profile at $\lambda = 11.5\ \mu m$ is given and field intensity is maximum at the edges. This can be attributed to the singular behavior of electric field near sharp edges. That the field intensity

is 0 in the base ZnO and the Si substrate shows that the incident light is not coupled into the substrate layer through the grating waveguide effect.

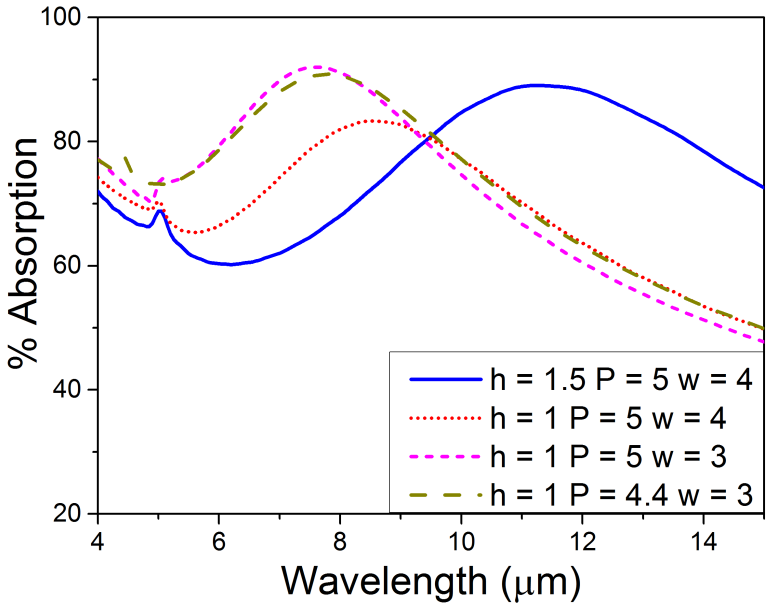

Figure 4.4: Absorption spectra for different structures. As other plasmonic devices demonstrated using conventional metals, ZnO absorber allows the spectra to be tuned.

Finally a parameter sweep is conducted in order to investigate the structural dependence of the absorption spectra (Figure 4.4). When $P = 5\ \mu m$, there is a resonance at 5 μm as expected and when $P = 4.4\ \mu m$, the resonance shifts to 4.4 μm. Also, Figure 4.4 shows that the wavelength of the broadband resonance is affected both by w and h. The grating width (w) determines the plasmon wavevector along the slot waveguide [67] and the height of the grating affects the supported mode [66]. As other plasmonic devices demonstrated using conventional metals, ZnO absorber allows the spectra to be tuned [15].

In Figure 4.3, the significant contribution of plasmons to the absorption spectra is clear. Also, Figure 4.4 shows that the resonances can be tuned. Therefore, the structure can be tailored to achieve maximum absorption in a desired spectral range. An optimum design is sought in order to maximize the average absorption in 4-15 μm band. The period of the structure is varied from 1 μm to 5 μm, and the height of the gratings are swept from 0.5 μm to 1.5 μm. For each of these two

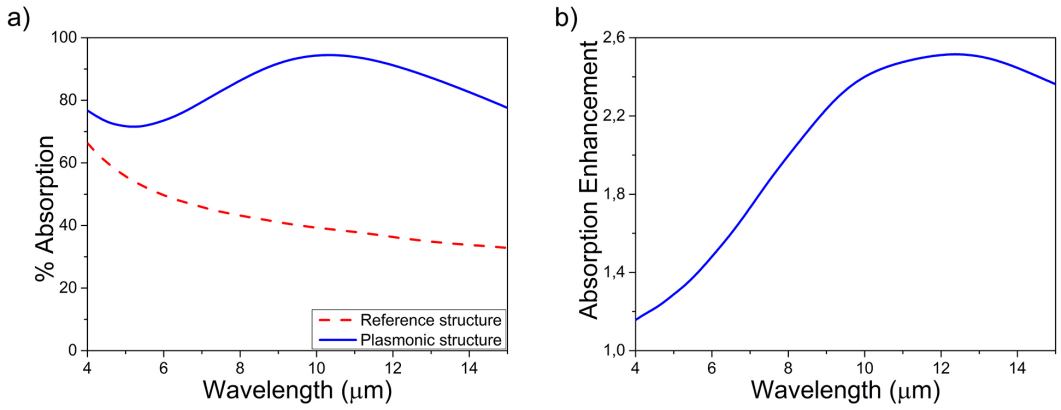

Figure 4.5: a) Comparison of the absorption spectra of the reference structure and the plasmonic structure when $h = 1.4\ \mu m$, $P = 1.8\ \mu m$ and $w = 1.2\ \mu m$. b) Absorption enhancement is the ratio of % absorption of plasmonic structure to the % absorption of the reference structure.

parameters, the width of the gratings is also varied where the minimum width is 100 nm and the maximum width is the 80% of the corresponding period. The base thickness of ZnO was kept constant, i.e. 1 μm. For each structure, reference structures are also created where a slab of flat ZnO that has the same thickness is placed on Si substrate. For both sets of structures, absorption in the 4-15 μm band are calculated. When the grating has a height of 1.4 μm, a period of 1.8 μm and a width of 1.2 μm; the absorption is maximized. The absorption spectra of this structure is given on Figure 4.5. For the entire spectrum, absorption is over 70% and the average absorption in this spectrum is $\sim$ 85%.

4.2 ZnO for Uncooled Infrared Imaging

Vision is humankind's dominant sense as it is where most of the information about the surrounding environment is derived from [68]. Therefore, the desire to see under darkness is obvious.

The visual spectrum (VIS) is a narrow band in the entire electromagnetic spectrum of optical frequencies. Some IR wavelengths can also be used for imaging purposes if necessary devices are designed. The transmittance of the atmosphere surrounding our world is a function of the wavelength. Due to the vibrational modes of the gases, atmosphere is only transparent at a number of bands in the IR and these bands are where imaging can be achieved. These are short-wave IR (SWIR, 0.7-2 μm), mid-wave IR (MWIR, 3-5 μm) and long-wave IR (LWIR, 8-12 μm).

Imaging in the SWIR is similar to VIS since at these wavelengths imaging depends on light that is reflected from the objects. However, imaging in MWIR and LWIR depends on the detection of light that is emitted from the objects. Any object that is not at absolute zero temperature (0 °K) emits light and this emission depends on the temperature of the material. The peak wavelength of emission of the Sun, which is around 6000 °K, is at around 500 nm, i.e. roughly the center of the visible spectrum. This peak wavelength is around 10 μm for objects at near room temperature and at shorter wavelengths for hotter objects. This fact makes the imaging in the LWIR (8-12 μm) favorable.

As mentioned before, special detectors need to be designed for imaging in the IR. These detectors can be classified under two types: cooled and uncooled photodetectors.

The cooled photodetectors are semiconductor optoelectronic devices that operate on photogeneration and collection of electrons and holes. Although these devices can be simple diodes fabricated using low bandgap semiconductors like mercury cadmium telluride (HgCdTe) and indium antimonide (InSb), there are also more complex structures like quantum well infrared photodetectors (QWIP)

and type-II superlattice photodiodes. These photodetectors offer high performance (higher resolution, higher signal-to-noise ratio, faster response) compared to the uncooled counterparts. But, they need to be cooled to cryogenic temperatures because the thermal generation of electrons and holes at room temperature is much greater than the photogeneration. This increases the cost of cooled photodetectors which hinders the integration of IR imaging with the civilian life.

The working principle of the uncooled detectors is different. They sense the temperature change due to the absorption of the IR radiation and there is no need for cooling. Uncooled detectors offer cost effective solutions targeting the competitive high volume low-end user market. With the development of new and cheaper detectors, IR imaging market is shifting from defense to civilian sectors with the introduction of new commercial and high volume markets such as automotive, surveillance, thermography, and IR imaging in smartphones (Figure 4.6) [69].

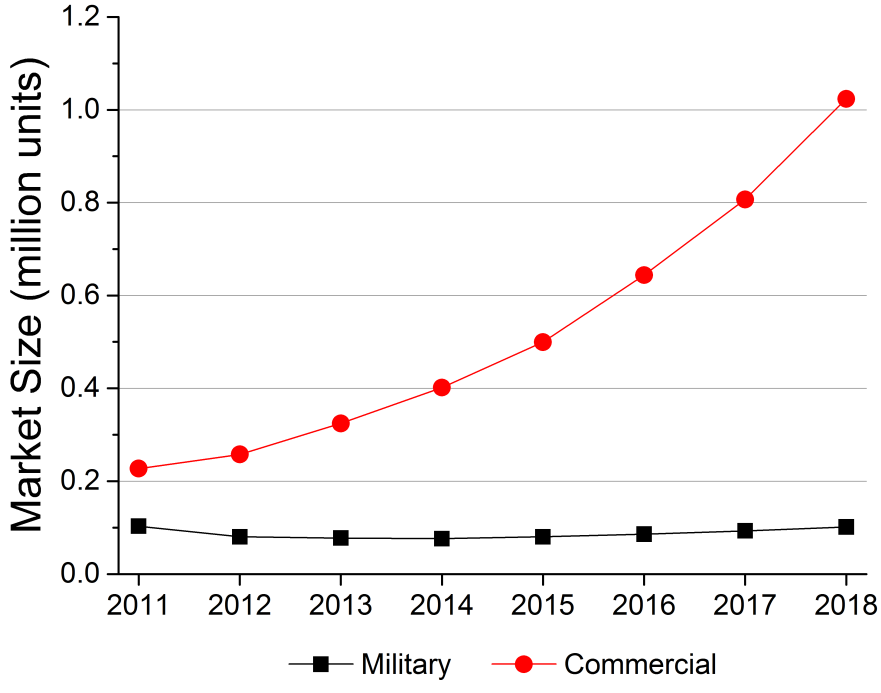

Figure 4.6: Global uncooled thermal camera market size forecast in units

Among uncooled detectors such as thermopiles, pyroelectric detectors, and microbolometers, the latter are more popular for infrared imaging purposes [70].

A microbolometer pixel consists of an absorber layer, an active detector material (thermistor), and the support arms as given in Figure 4.7 [71]. The absorber layer and the thermistor are free-standing for thermal isolation. The absorption of the incident radiation causes an increase in the temperature of the thermistor. This temperature increase changes the resistance of the thermistor, and this change is converted to electrical signal by the read-out integrated circuit (ROIC). The percentage of change in the resistance of the thermistor per kelvin is given by the *temperature coefficient of resistance* (TCR) of the thermistor material.

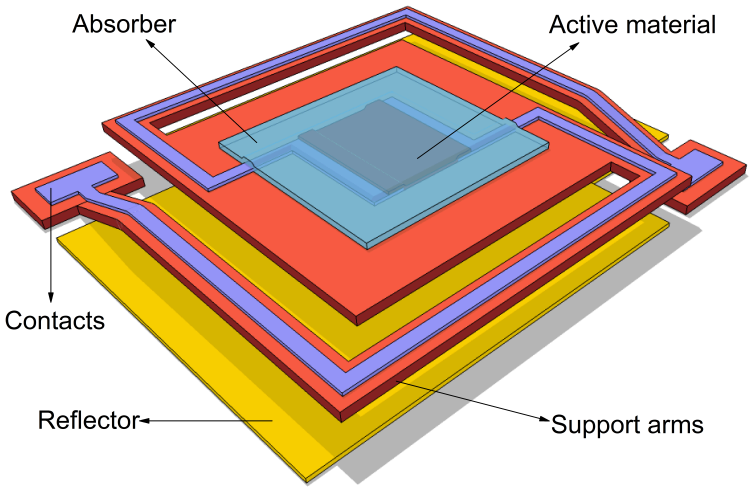

Figure 4.7: Schematic of a conventional microbolometer

The key figure of merit indicating the performance of a microbolometer is the *noise equivalent temperature difference* (NETD) which is defined as the change of temperature of the scene that will cause an increase of signal-to-noise ratio by unity. NETD is given by [72]

$$NETD = \frac{4F^2 V_n}{\tau_o A \mathcal{R} (\Delta P/\Delta T)_{\lambda_1 - \lambda_2}} \tag{4.2}$$

where F is the focal ratio of the optics, V_n is the total electrical noise, τ_o is the transmittance of the optics, A is the area and $\mathcal{R}$ is the responsivity of the pixel, $(\Delta P/\Delta T)_{\lambda_1 - \lambda_2}$ is the change of power per unit area radiated by a blackbody at

temperature T, measured within the spectral band of $(\lambda_1 - \lambda_2)$. The responsivity can be expressed as

$$\mathcal{R} = \frac{\Delta V}{P_o} = \frac{\eta I_d \alpha R_d}{G_{th}} \tag{4.3}$$

where η is the absorption coefficient, I_d is the detector current, α is the TCR, R_d is the detector resistance, G_{th} is the thermal conductance. Another important parameter affected by the thermal conductance is the time constant of the detector which is given by

$$\tau = \frac{C_{th}}{G_{th}} \tag{4.4}$$

where C_{th} is the thermal capacitance. The time constant is a measure of the response time of the microbolometer, and a smaller time constant is desirable for faster sensors. For imaging applications based on 30 Hz frame rate, a time constant of 10 ms is tolerable and that for 60 Hz frame rate should be less than 7 ms [73].

In order to maximize the responsivity of the microbolometer and reduce the NETD, new materials or sensors architectures that provide higher TCR and absorptivity and lower thermal conductivity are desirable. However, when thermal conductance, G_{th}, is lower, the time constant increases. Due to the trade-off between NETD and time constant, a new figure of merit is defined [74], NETD-thermal time constant product

$$FOM = NETD \times \tau \tag{4.5}$$

In terms of thermistor materials, most of the commercially available microbolometers employ vanadium oxide (VO_x) and amorphous silicon ($\alpha - Si$) with TCR values between -2 %/K and -3 %/K [70, 71]. In addition, alternative active materials reported include but are not limited to thin film metals such as titanium (0.35 %/K) [75] and platinum (0.14 %/K) [76], and YBaCuO (-3.3 %/K) [77]. Also, recently, researchers in our group demonstrated atomic layer deposition (ALD) grown ZnO as a candidate thermistor material with a TCR value of -10.4 %/K [57]. While the most widely used absorber layer is Si_3N_4 [78–80] there are also reports on the use of alternative CMOS compatible dielectrics [81] and thin metals [72, 76] as the absorber layer.

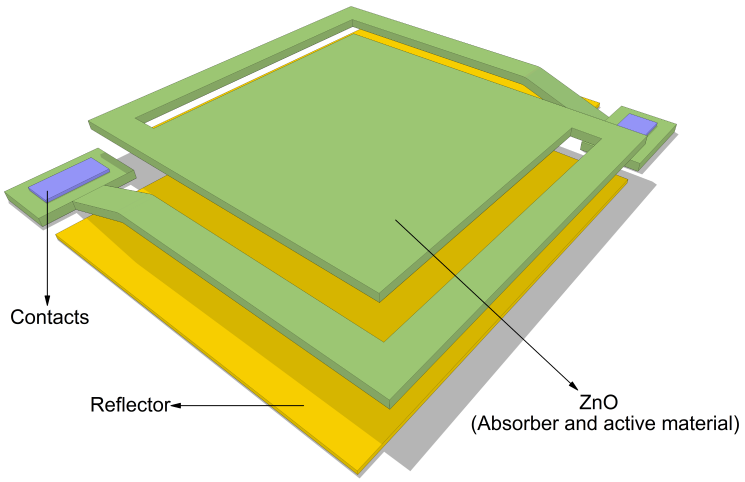

Figure 4.8: Schematic of the proposed single layer all-ZnO microbolometer structure

The material complexity and process steps of microbolometers could be reduced if the thermistor layer and the absorber layer were consolidated in a single layer. Recently, Yoneoka et. al. suggested replacing the thermistor and absorber layers with a thin ALD grown Pt layer [76]. It was mentioned that the TCR value of ALD grown ZnO (grown at 120 °C) was measured to be -10.4 %/K [57]. Also, the optical properties of ZnO was already extracted in this thesis. Therefore, an all-ZnO microbolometer, where ALD-grown ZnO layer is employed as both the thermistor and the absorber as shown in Figure 4.8 is computationally analyzed using FDTD method in order to calculate the absorptivity in the long-wave infrared (LWIR) region (8-12 μm). The results of the optical simulations are fed into thermal simulations and time constant and NETD values are extracted.

4.2.1 Optical Simulations

For simplicity, a 2D simulation setup is chosen in which the arms and anchors features of a standard microbolometer are neglected as can be seen in Figure 4.9. On the x-axis, periodic boundary conditions are assumed. On the y-axis, metal boundary condition is chosen at the bottom, to represent the metallic

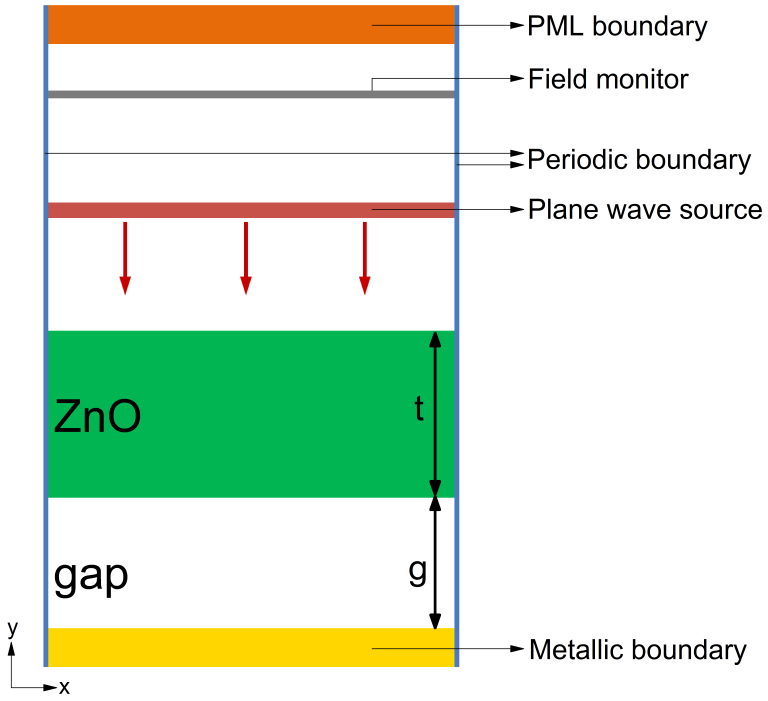

Figure 4.9: Simulation setup for the all-ZnO microbolometer structure

reflector beneath the gap. Metal boundary conditions are perfectly reflecting and do not allow electromagnetic energy to escape the simulation area. On the top, a perfectly matched layer (PML) is assumed. The mesh step in the y direction is 25 nm. In the x direction, only one mesh is used due to the periodicity. The structure is illuminated with a normally incident plane wave where the wavelength range of the light is 3-15 μm. A field monitor is placed behind the plane wave source in order to calculate the absorption in the microbolometer structure. Since all energy incident at the bottom boundary is reflected back, total absorption can be calculated using P_{abs}=$(1 - P_{ref})$ where P_{ref} is the ratio of the power transmitted through the field monitor to the power radiated by the plane wave source. Therefore, P_{abs} gives the ratio of absorbed energy to incident energy.

A parameter sweep is conducted to find the optimum structure for which the average absorption in the 8-12 μm band is maximized. The thickness of the ZnO film (t) is varied from 50 nm to 2 μm and the gap height (g) is varied from 100 nm to 4 μm. Average absorption in the LWIR band is calculated by equally weighing absorption at all wavelengths in the 8-12 μm band (Figure 4.10).

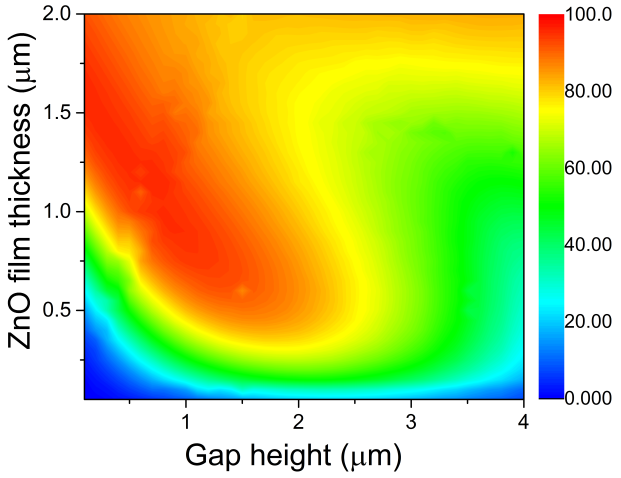

Figure 4.10: Average percent absorption in the LWIR (8-12 μm) band vs simulation parameters i.e. ZnO film thickness and gap height.

According to Figure 4.10, it can be stated that; in general, as t increases, the average absorption increases as expected. Average absorption is maximized when t is between 1.25-2 μm. This is due to the Fabry-Perrot resonance inside the ZnO film. The resonance condition for the Fabry-Perrot cavity is fulfilled when the cavity length is one fourth of the wavelength of the incident light. When the incident light is in the LWIR band ($8\ \mu m < \lambda_o < 12\ \mu m$), the wavelength inside the ZnO film is in the 4.5-8 μm range since $\lambda = \lambda_o/n$ where n is the refractive index of ZnO at the corresponding wavelength (Figure 4.11). Therefore when the film thickness is in the 1.25-2 μm range, the resonant wavelength is between 8-12 μm and this leads to an efficient absorption in the LWIR band.

Besides the film itself, the resonant cavity can be formed by the gap beneath. Here, the medium is vacuum and therefore the resonance occurs when the gap height is between 2-3 μm ($\lambda_o/4$). Adjusting the gap height between 2-3 μm, more than 40% absorption is achieved even with ZnO films as thin as 100 nm. In Figure 4.10, note that, absorption is almost zero for very thin ($<$ 100 nm) absorbing layers if the gap height is below 2 μm. Finally, the results show that maximum absorption (95.6%) occurs when $t = 1.1\ \mu m$ and $g = 0.8\ \mu m$.

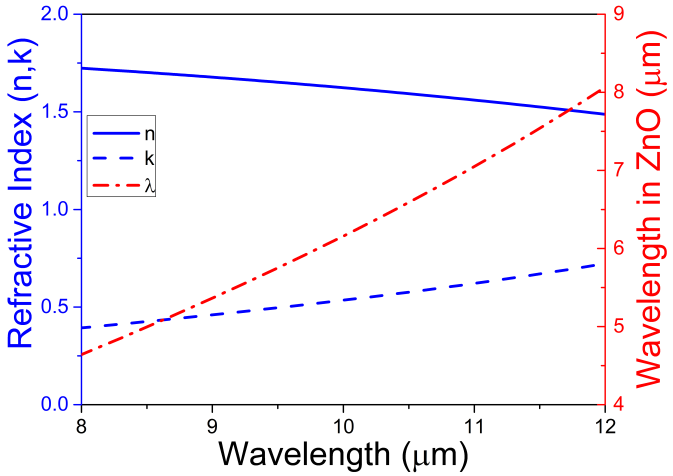

Figure 4.11: On the left axis, real (n) and imaginary (k) parts of refractive index of ZnO (grown at 120°C) in LWIR region is given. On the right axis, wavelength of light in ZnO film is given ($\lambda = \lambda_o/n$).

4.2.2 Thermal Simulations

In order to extract the figures of merit of the all-ZnO microbolometer, thermal simulations are conducted by Dr. Yusuf Tanrikulu at Adana Science and Technology University. For the simulations, the density of ZnO is assumed as 5.6 g/cm^3 [82] and thermal conductivity is assumed to be 90 W/mK [83]. For the specific heat of ZnO, the value given on [84] is used, 40.25 $J/mol.K$ ($0.49 J/gK$). Table 4.1 shows the thermal simulation results for different pixel structures with varying ZnO film thickness and gap height. Also, in some of the simulations, the arm thickness of the microbolometer is thinner than the ZnO film. The aim is reducing the thermal conductance and therefore increasing the responsivity, $\mathcal{R}$. Increased responsivity results in lower NETD as can be seen in equations (4.2) and (4.3).

The highest performing detector (NETD of 171 mK) can be obtained with a body thickness of 1.1 μm and an arm thickness of 50 nm. The fastest detector ($\tau = 0.32$ ms) is achieved with a ZnO thickness of 150 nm both on the body and the arms. The rows representing these detectors are highlighted on Table 4.1.

Table 4.1: NETD and thermal time constant calculation for different pixels using the results of the optical and thermal simulations.

Arm Thickness (μm)	Film Thickness (μm)	Gap Height (μm)	NETD (mK)	Time constant (ms)	FOM (mK.ms)
1.10	1.10	0.8	3575	0.33	1180
0.05	1.10	0.8	171	6.60	1129
0.15	0.15	2.1	940	0.32	301
0.05	0.40	1.7	198	2.50	495
0.05	0.25	2.0	239	1.70	406
0.05	0.15	2.1	325	0.92	299

In conclusion, an all-ZnO microbolometer is introduced and two distinct pixel designs are presented: The detector design with the highest absorption offers an NETD value of 171 mK with a thermal time constant of 6.6 ms, and FOM (NETD-time constant product) of 1129 mK.ms. Although the thermal time constant is compatible with 60 Hz frame rate imaging, this detector is outperformed by the highest performance microbolometers available in today's technology that achieve $<$ 50 mK NETD. Nevertheless, such a microbolometer can be used in low-end applications such as thermography and automotive.

The fastest detector design shows 0.32 ms thermal time constant with an NETD of 940 mK and FOM of 301 mK.ms. This detector is suitable for applications where the speed is of the primary importance such as missile tracking. This application does not require a very low NETD value since the object to be tracked (a missile nozzle in this case) is a lot hotter than the scene.

Chapter 5

Conclusion and Future Directions

In conclusion, ALD grown ZnO is introduced as an alternative plasmonic material in the infrared. The dielectric permittivity values of ZnO grown at different temperatures are extracted and it is shown that the plasma frequency of ALD grown ZnO depends on growth temperature. The ability to tune the optical properties enables effective optimization of propagation loss and mode confinement width of plasmonic devices. Furthermore, a plasmonic grating coupler is simulated using FDTD method and plasmonic resonances at the ZnO/air interface are demonstrated. The absorption spectrum of the simulated device show exceptional performance enhancement over reference device in the 4-15 μm wavelength band. The future work will be fabricating grating structures using focused ion beam (FIB) and experimentally demonstrating the plasmonic resonances at ALD grown ZnO.

Consolidating absorber and thermistor layers within a single ZnO layer, the main advantage of the all-ZnO microbolometer is the reduced material complexity and number of fabrication steps. This advantage leads to higher yield and taking into account the simple growth technology offered by ALD, all-ZnO microbolometer appears as a low cost alternative. The future work about ZnO bolometers will be the realization of this microbolometer.

Bibliography

[1] H. A. Atwater, "The promise of plasmonics," *Scientific American*, vol. 296, no. 4, pp. 56–62, 2007.

[2] R. W. Wood, "Xlii. on a remarkable case of uneven distribution of light in a diffraction grating spectrum," *Philosophical Magazine Series 6*, vol. 4, no. 21, pp. 396–402, 1902.

[3] T. W. Ebbesen, H. Lezec, H. Ghaemi, T. Thio, and P. Wolff, "Extraordinary optical transmission through sub-wavelength hole arrays," *Nature*, vol. 391, no. 6668, pp. 667–669, 1998.

[4] E. Ozbay, "Plasmonics: Merging photonics and electronics at nanoscale dimensions," *Science*, vol. 311, no. 5758, pp. 189–193, 2006.

[5] M. I. Stockman, "Nanoplasmonics: past, present, and glimpse into future," *Optics Express*, vol. 19, no. 22, pp. 22029–22106, 2011.

[6] D. F. P. Pile, T. Ogawa, D. K. Gramotnev, T. Okamoto, M. Haraguchi, M. Fukui, and S. Matsuo, "Theoretical and experimental investigation of strongly localized plasmons on triangular metal wedges for subwavelength waveguiding," *Applied Physics Letters*, vol. 87, no. 6, p. 061106, 2005.

[7] S. Kawata, Y. Inouye, and P. Verma, "Plasmonics for near-field nano-imaging and superlensing," *Nature Photonics*, vol. 3, no. 7, pp. 388–394, 2009.

[8] W. Srituravanich, N. Fang, C. Sun, Q. Luo, and X. Zhang, "Plasmonic nanolithography," *Nano Letters*, vol. 4, no. 6, pp. 1085–1088, 2004.

[9] E. Battal and A. K. Okyay, "Metal-dielectric-metal plasmonic resonators for active beam steering in the infrared," *Optics Letters*, vol. 38, no. 6, pp. 983–985, 2013.

[10] S.-W. Qu and Z.-P. Nie, "Plasmonic nanopatch array for optical integrated circuit applications," *Scientific Reports*, vol. 3, 2013.

[11] K. Chen, R. Adato, and H. Altug, "Dual-band perfect absorber for multispectral plasmon-enhanced infrared spectroscopy," *ACS Nano*, vol. 6, no. 9, pp. 7998–8006, 2012.

[12] R. Adato, A. A. Yanik, J. J. Amsden, D. L. Kaplan, F. G. Omenetto, M. K. Hong, S. Erramilli, and H. Altug, "Ultra-sensitive vibrational spectroscopy of protein monolayers with plasmonic nanoantenna arrays," *Proceedings of the National Academy of Sciences*, vol. 106, no. 46, pp. 19227–19232, 2009.

[13] H. A. Atwater and A. Polman, "Plasmonics for improved photovoltaic devices," *Nature Materials*, vol. 9, no. 3, pp. 205–213, 2010.

[14] F. B. Atar, E. Battal, L. E. Aygun, B. Daglar, M. Bayindir, and A. K. Okyay, "Plasmonically enhanced hot electron based photovoltaic device," *Optics Express*, vol. 21, no. 6, pp. 7196–7201, 2013.

[15] M. Pu, C. Hu, M. Wang, C. Huang, Z. Zhao, C. Wang, Q. Feng, and X. Luo, "Design principles for infrared wide-angle perfect absorber based on plasmonic structure," *Optics Express*, vol. 19, no. 18, pp. 17413–17420, 2011.

[16] J. Hao, L. Zhou, and M. Qiu, "Nearly total absorption of light and heat generation by plasmonic metamaterials," *Physical Review B*, vol. 83, no. 16, p. 165107, 2011.

[17] G. V. Naik, V. M. Shalaev, and A. Boltasseva, "Alternative plasmonic materials: beyond gold and silver," *Advanced Materials*, vol. 25, no. 24, pp. 3264–3294, 2013.

[18] J. B. Khurgin and A. Boltasseva, "Reflecting upon the losses in plasmonics and metamaterials," *MRS Bulletin*, vol. 37, no. 08, pp. 768–779, 2012.

[19] G. V. Naik, *New Materials And Devices For Plasmonics And Metamaterial Applications*. PhD thesis, Purdue University, 2013.

[20] J.-S. G. Bouillard, W. Dickson, D. P. O?Connor, G. A. Wurtz, and A. V. Zayats, "Low-temperature plasmonics of metallic nanostructures," *Nano Letters*, vol. 12, no. 3, pp. 1561–1565, 2012.

[21] Y. E. Kesim, E. Battal, and A. K. Okyay, "Plasmonic materials based on zno films and their potential for developing broadband middle-infrared absorbers," *AIP Advances*, vol. 4, no. 7, pp. –, 2014.

[22] A. Fazzio, M. J. Caldas, and A. Zunger, "Electronic structure of copper, silver, and gold impurities in silicon," *Phys. Rev. B*, vol. 32, pp. 934–954, Jul 1985.

[23] D.-G. Park, T.-H. Cha, K.-Y. Lim, H.-J. Cho, T.-K. Kim, S.-A. Jang, Y.-S. Suh, V. Misra, I.-S. Yeo, J.-S. Roh, *et al.*, "Robust ternary metal gate electrodes for dual gate cmos devices," in *Electron Devices Meeting, 2001. IEDM'01. Technical Digest. International*, pp. 30–6, IEEE, 2001.

[24] G. V. Naik, J. Kim, and A. Boltasseva, "Oxides and nitrides as alternative plasmonic materials in the optical range [invited]," *Optical Materials Express*, vol. 1, no. 6, pp. 1090–1099, 2011.

[25] M. Wu, Z. Han, and V. Van, "Conductor-gap-silicon plasmonic waveguides and passive components at subwavelength scale," *Opt. Express*, vol. 18, pp. 11728–11736, May 2010.

[26] D. Dai and S. He, "A silicon-based hybrid plasmonic waveguide with a metal cap for a nano-scale light confinement," *Optics Express*, vol. 17, no. 19, pp. 16646–16653, 2009.

[27] A. V. Krasavin and A. V. Zayats, "Silicon-based plasmonic waveguides," *Optics Express*, vol. 18, no. 11, pp. 11791–11799, 2010.

[28] J. A. Dionne, L. A. Sweatlock, M. T. Sheldon, A. P. Alivisatos, and H. A. Atwater, "Silicon-based plasmonics for on-chip photonics," *Selected Topics in Quantum Electronics, IEEE Journal of*, vol. 16, no. 1, pp. 295–306, 2010.

[29] R. F. Pierret, *Semiconductor Device Fundamentals*. Addison-Wesley, 1996.

[30] F. A. Trumbore, "Solid solubilities of impurity elements in germanium and silicon*," *Bell System Technical Journal*, vol. 39, no. 1, pp. 205–233, 1960.

[31] Y. Kang, H.-D. Liu, M. Morse, M. J. Paniccia, M. Zadka, S. Litski, G. Sarid, A. Pauchard, Y.-H. Kuo, H.-W. Chen, *et al.*, "Monolithic germanium/silicon avalanche photodiodes with 340 ghz gain–bandwidth product," *Nature Photonics*, vol. 3, no. 1, pp. 59–63, 2009.

[32] J. Kim, G. Naik, N. Emani, U. Guler, and A. Boltasseva, "Plasmonic resonances in nanostructured transparent conducting oxide films," *Selected Topics in Quantum Electronics, IEEE Journal of*, vol. 19, pp. 4601907–4601907, May 2013.

[33] S. Q. Li, P. Guo, L. Zhang, W. Zhou, T. W. Odom, T. Seideman, J. B. Ketterson, and R. P. Chang, "Infrared plasmonics with indium–tin-oxide nanorod arrays," *ACS Nano*, vol. 5, no. 11, pp. 9161–9170, 2011.

[34] M. Kanehara, H. Koike, T. Yoshinaga, and T. Teranishi, "Indium tin oxide nanoparticles with compositionally tunable surface plasmon resonance frequencies in the near-ir region," *Journal of the American Chemical Society*, vol. 131, no. 49, pp. 17736–17737, 2009.

[35] S. Franzen, "Surface plasmon polaritons and screened plasma absorption in indium tin oxide compared to silver and gold," *The Journal of Physical Chemistry C*, vol. 112, no. 15, pp. 6027–6032, 2008.

[36] S. H. Brewer and S. Franzen, "Optical properties of indium tin oxide and fluorine-doped tin oxide surfaces: correlation of reflectivity, skin depth, and plasmon frequency with conductivity," *Journal of Alloys and Compounds*, vol. 338, no. 1, pp. 73–79, 2002.

[37] G. V. Naik, J. Liu, A. V. Kildishev, V. M. Shalaev, and A. Boltasseva, "Demonstration of al: Zno as a plasmonic component for near-infrared metamaterials," *Proceedings of the National Academy of Sciences*, vol. 109, no. 23, pp. 8834–8838, 2012.

[38] A. Grigorenko, M. Polini, and K. Novoselov, "Graphene plasmonics," *Nature Photonics*, vol. 6, no. 11, pp. 749–758, 2012.

[39] L. Ju, B. Geng, J. Horng, C. Girit, M. Martin, Z. Hao, H. A. Bechtel, X. Liang, A. Zettl, Y. R. Shen, *et al.*, "Graphene plasmonics for tunable terahertz metamaterials," *Nature Nanotechnology*, vol. 6, no. 10, pp. 630–634, 2011.

[40] F. H. Koppens, D. E. Chang, and F. J. Garcia de Abajo, "Graphene plasmonics: a platform for strong light–matter interactions," *Nano Letters*, vol. 11, no. 8, pp. 3370–3377, 2011.

[41] M. Jablan, H. Buljan, and M. Soljačić, "Plasmonics in graphene at infrared frequencies," *Physical Review B*, vol. 80, no. 24, p. 245435, 2009.

[42] E. H. Hwang and S. Das Sarma, "Dielectric function, screening, and plasmons in two-dimensional graphene," *Phys. Rev. B*, vol. 75, p. 205418, May 2007.

[43] C. A. Balanis, *Advanced Engineering Electromagnetics*. John Wiley & Sons, 2012.

[44] A. E. Siegman, *Lasers*. University Science Books, 1986.

[45] J. William D. Callister, *Materials Science and Engineering: an Introduction*. John Wiley & Sons, 2007.

[46] M. A. Ordal, R. J. Bell, R. W. Alexander, L. L. Long, and M. R. Querry, "Optical properties of fourteen metals in the infrared and far infrared: Al, co, cu, au, fe, pb, mo, ni, pd, pt, ag, ti, v, and w.," *Appl. Opt.*, vol. 24, pp. 4493–4499, Dec 1985.

[47] M. G. Blaber, M. D. Arnold, and M. J. Ford, "Search for the ideal plasmonic nanoshell: The effects of surface scattering and alternatives to gold and silver," *The Journal of Physical Chemistry C*, vol. 113, no. 8, pp. 3041–3045, 2009.

[48] L. A. Sweatlock, *Plasmonics: Numerical Methods and Device Applications*. PhD thesis, California Institute of Technology, 2008.

[49] S. A. Maier, *Plasmonics: Fundamentals and Applications*. Springer, 2007.

[50] A. Trugler, *Optical Properties of Metallic Nanoparticles*. PhD thesis, University of Graz, 2011.

[51] H. R. E. Kretschmann, "Radiative decay of non-radiative surface plasmons excited by light," *Z. Naturforschung*, vol. 23A, pp. 2135–2136, 1968.

[52] P. Berini, "Figures of merit for surface plasmon waveguides," *Opt. Express*, vol. 14, pp. 13030–13042, Dec 2006.

[53] H. Morkoc and U. Ozgur, *Zinc Oxide: Fundamentals, Materials and Device Technology*. Wiley-VCH Verlag GmbH & Co. KGaA, 2009.

[54] E. Guziewicz, M. Godlewski, L. Wachnicki, T. A. Krajewski, G. Luka, S. Gieraltowska, R. Jakiela, A. Stonert, W. Lisowski, M. Krawczyk, J. W. Sobczak, and A. Jablonski, "Ald grown zinc oxide with controllable electrical properties," *Semiconductor Science and Technology*, vol. 27, no. 7, p. 074011, 2012.

[55] J. A. Woollam Co., "Ellipsometry measurements." `http://www.jawoollam.com/tutorial_4.html`. Accessed: 10.06.2014.

[56] J. A. Woollam Co., Inc., *CompleteEASE Data Analysis Manual*.

[57] E. Battal, S. Bolat, M. Y. Tanrikulu, A. K. Okyay, and T. Akin, "Atomic layer deposited zinc-oxide as tunable uncooled infrared microbolometer material," *Physica Status Solidi (a)*, 2014. DOI: 10.1002/pssa.201431195.

[58] W. R. L. Lambrecht, A. V. Rodina, S. Limpijumnong, B. Segall, and B. K. Meyer, "Valence-band ordering and magneto-optic exciton fine structure in zno," *Phys. Rev. B*, vol. 65, p. 075207, Jan 2002.

[59] R. L. Olmon, B. Slovick, T. W. Johnson, D. Shelton, S.-H. Oh, G. D. Boreman, and M. B. Raschke, "Optical dielectric function of gold," *Physical Review B*, vol. 86, no. 23, p. 235147, 2012.

[60] K. S. Yee, "Numerical solution of initial boundary value problems involving maxwell?s equations," *IEEE Trans. Antennas Propag*, vol. 14, no. 3, pp. 302–307, 1966.

[61] M. G. Bray, *Finite-Difference Time-Domain Simulation of Electromagnetic Bandgap and Bi-Anisotropic Metamaterials*. PhD thesis, The Pennsylvania State University, 2005.

[62] L. Inc., "Fdtd solutions." `https://www.lumerical.com/tcad-products/fdtd/`. Accessed: 14.06.2014.

[63] P. Neutens, P. Van Dorpe, I. De Vlaminck, L. Lagae, and G. Borghs, "Electrical detection of confined gap plasmons in metal–insulator–metal waveguides," *Nature Photonics*, vol. 3, no. 5, pp. 283–286, 2009.

[64] M. W. McCutcheon and M. Loncar, "Design of a silicon nitride photonic crystal nanocavity with a quality factor of one million for coupling to a diamond nanocrystal," *Optics Express*, vol. 16, no. 23, pp. 19136–19145, 2008.

[65] G. Veronis and S. Fan, "Modes of subwavelength plasmonic slot waveguides," *Journal of Lightwave Technology*, vol. 25, no. 9, pp. 2511–2521, 2007.

[66] M. Bora, B. J. Fasenfest, E. M. Behymer, A. S. Chang, H. T. Nguyen, J. A. Britten, C. C. Larson, J. W. Chan, R. R. Miles, and T. C. Bond, "Plasmon resonant cavities in vertical nanowire arrays," *Nano Letters*, vol. 10, no. 8, pp. 2832–2837, 2010.

[67] J. Dionne, L. Sweatlock, H. Atwater, and A. Polman, "Plasmon slot waveguides: Towards chip-scale propagation with subwavelength-scale localization," *Physical Review B*, vol. 73, no. 3, p. 035407, 2006.

[68] N. J. Wade and M. Swanston, *Visual perception: an introduction*. Routledge, 1991.

[69] P. Danini and Y. De Charentenay, "Uncooled infrared imaging technology & market trends report," tech. rep., Yole Developpement, 2013.

[70] F. Niklaus, C. Vieider, and H. Jakobsen, "Mems-based uncooled infrared bolometer arrays: a review," *Proc. SPIE*, vol. 6836, pp. 68360D–68360D–15, 2007.

[71] M. Y. Tanrikulu, *An Uncooled Infrared Microbolometer Detector Array Using Surface Micromachined MEMS Technology*. PhD thesis, Middle East Technical University, 2007.

[72] P. W. Kruse and D. D. Skatrud, *Uncooled Infrared Imaging Arrays and Systems*. Academic Press, 1997.

[73] B. Fique, J. Tissot, C. Trouilleau, A. Crastes, and O. Legras, "Uncooled microbolometer detector: Recent developments at ulis," *Infrared Physics & Technology*, vol. 49, no. 3, pp. 187 – 191, 2007. Workshop on Advanced Infrared Technology and Applications.

[74] M. Kohin and N. R. Butler, "Performance limits of uncooled vox microbolometer focal plane arrays," *Proc. SPIE*, vol. 5406, pp. 447–453, 2004.

[75] A. Tanaka, S. Matsumoto, N. Tsukamoto, S. Itoh, K. Chiba, T. Endoh, A. Nakazato, K. Okuyama, Y. Kumazawa, M. Hijikawa, H. Gotoh, T. Tanaka, and N. Teranishi, "Infrared focal plane array incorporating silicon ic process compatible bolometer," *Electron Devices, IEEE Transactions on*, vol. 43, pp. 1844–1850, Nov 1996.

[76] S. Yoneoka, M. Liger, G. Yama, R. Schuster, F. Purkl, J. Provine, F. Prinz, R. Howe, and T. Kenny, "Ald-metal uncooled bolometer," in *Micro Electro Mechanical Systems (MEMS), 2011 IEEE 24th International Conference on*, pp. 676–679, Jan 2011.

[77] A. Jahanzeb, C. M. Travers, Z. Celik-Butler, D. P. Butler, and S. G. Tan, "A semiconductor ybacuo microbolometer for room temperature ir imaging," *Electron Devices, IEEE Transactions on*, vol. 44, no. 10, pp. 1795–1801, 1997.

[78] S. Z. Lulec, S. E. Kucuk, E. Battal, A. K. Okyay, M. Y. Tanrikulu, and T. Akin, "An analysis for the broad-band absorption enhancement using

plasmonic structures on uncooled infrared detector pixels," in *SPIE Defense, Security, and Sensing*, pp. 83531D–83531D, International Society for Optics and Photonics, 2012.

[79] W. A. Radford, R. Wyles, J. Wyles, J. B. Varesi, M. Ray, D. F. Murphy, A. Kennedy, A. Finch, E. A. Moody, F. Cheung, *et al.*, "Microbolometer uncooled infrared camera with 20-mk netd," in *SPIE's International Symposium on Optical Science, Engineering, and Instrumentation*, pp. 636–646, International Society for Optics and Photonics, 1998.

[80] O. Erturk, E. Battal, S. E. Kucuk, A. K. Okyay, and T. Akin, "A plasmonically enhanced pixel structure for uncooled microbolometer detectors," in *Infrared Technology and Applications XXXIX*, vol. 8704, pp. 87041E–87041E–7, International Society for Optics and Photonics, 2013.

[81] D. S. Tezcan, S. Eminoglu, and T. Akin, "A low-cost uncooled infrared microbolometer detector in standard cmos technology," *Electron Devices, IEEE Transactions on*, vol. 50, no. 2, pp. 494–502, 2003.

[82] R. C. Weast, M. J. Astle, and W. H. Beyer, *CRC Handbook of Chemistry and Physics*, vol. 69. CRC press Boca Raton, FL, 1988.

[83] J. Alvarez-Quintana, E. Martínez, E. Pérez-Tijerina, S. Pérez-García, and J. Rodríguez-Viejo, "Temperature dependent thermal conductivity of polycrystalline zno films," *Journal of Applied Physics*, vol. 107, no. 6, p. 063713, 2010.

[84] I. Z. Association, "Zinc oxide properties." `http://www.zinc.org/info/zinc_oxide_properties`. Accessed: 14.03.2014.